The Pennsylvania State University

The Graduate School

College of Engineering

# FLAME RESPONSE MECHANISMS AND THEIR INTERACTION IN A LEAN PREMIXED SWIRL-STABILIZED GAS TURBINE COMBUSTOR

A Thesis in

Mechanical Engineering

by

Brian Jones



Submitted in Partial Fulfillment
of the Requirements
for the Degree of

Master of Science

May 2011

The thesis of Brian Jones was reviewed and approved* by the following:

Domenic A. Santavicca
Professor of Mechanical Engineering
Thesis Advisor

Stephen R. Turns
Professor of Mechanical Engineering

Karen A. Thole
Professor of Mechanical Engineering
Head of the Department of Mechanical and Nuclear Engineering

*Signatures are on file in the Graduate School

## ABSTRACT

To satisfy increasingly stringent environmental regulations, gas turbine engines are run in a lean premixed mode. Unfortunately, operating in this mode greatly increases the flame's susceptibility to self sustained combustion instabilities. It is vital to understand flame dynamics in order to better predict the onset of such instabilities. At low velocity forcing amplitudes, there are two local flame response mechanisms that affect lean premixed flames: vorticity fluctuations affecting local flame wrinkling, and velocity fluctuations affecting the mean flame surface area. No experimental studies investigating the interaction of these mechanisms and their affect on the global flame response have been reported in the literature.

An experimental study was conducted to determine the effect of the interaction of these two flame response mechanisms on the global turbulent flame response in a lean premixed, swirl-stabilized gas turbine combustor. Premixed natural gas and air were modulated with a siren type modulation device at frequencies between 80 Hz and 360 Hz. Overall chemiluminescence intensity was recorded with photomultiplier tubes equipped with filters for CH*, $CO_2$*, and OH*, and used as a measure of the global flame heat release rate. Hot wire anemometry was used to measure the inlet velocity fluctuation. To characterize flame structure, flame length and shape, CH* chemiluminescence images were recorded at forced and unforced conditions. From chemiluminescence images synchronized in phase with the inlet velocity fluctuation, it was possible to characterize the role of the two flame response mechanisms.

Flame transfer function (FTF) measurements, which quantify the ratio of the flame's heat release rate response to inlet velocity fluctuations, were made for mean flow velocities of 20 m/s, 25 m/s, and 30 m/s, and equivalence ratios of 0.65, 0.70, 0.75, 0.80 with a normalized velocity forcing amplitude of 5%. It was found that the FTF gain and phase depend on mean velocity, flame length, and flame shape. Particularly interesting, a forcing frequency, defined as

$f_{min}$, was observed at which there was minimal heat release rate response. This frequency changed with the same parameters that influence the FTF measurements.

Chemiluminescence images revealed two general flame shapes: a typical "V" flame shape and a longer length "V" flame shape with an extension into the corner recirculation zone. Images phase synchronized with the input velocity fluctuation were taken for operating conditions representative of the two flame shapes. For a typical "V" flame, it was revealed that high FTF gain forcing frequency conditions exhibited a constructive interaction of the two flame response mechanisms. Operating conditions with forcing frequencies of minimal gain, $f_{min}$, exhibited a destructive interaction of the two mechanisms. For the longer "V" flame shape with an extension into the corner recirculation zone, it was found that the relative magnitude of the two flame response mechanisms, in addition to the phase relationship, significantly impacted the global flame heat release rate response. The vorticity disturbance mechanism was the preferred flame response mechanism for this flame shape.

Chemiluminescence measurements were also made at variable velocity forcing amplitudes. At a forcing frequency of $f_{min}$, it was shown that the heat release rate response would linearly increase above a null response once a normalized velocity forcing amplitude threshold was reached, starting at 10%. Vortex shedding was observed for amplitudes greater than 20%.

# TABLE OF CONTENTS

# LIST OF FIGURES

# LIST OF TABLES

# ACKNOWLEDGEMENTS

I would like to thank my advisor Professor Domenic Santavicca for his support and encouragement. I would also like to thank Professor Stephen Turns for reviewing this thesis. I sincerely appreciate all the help and feedback I received from Dr. Jong Guen Lee and Dr. Bryan Quay. Also, I wish to acknowledge my fellow graduate student lab members: Hyung Ju, Kyu Tae, Mike, Nick, Poravee, Simon, and Steve for their camaraderie and assistance. I thank John Raiser, Larry Horner, Sally Mills, and Virginia Smith for preparing experimental hardware and assisting with office work. Finally, I wish to thank all my family and friends for their support.

# Chapter 1

# Introduction

## 1.1 Motivation

Gas turbine engines for power generation and propulsion applications traditionally used diffusion flame combustors because of reliable performance and stability. This type of combustor, however, had the unfortunate drawback of producing excessive thermal $NO_x$ emission levels. To satisfy stringent restrictions on such emissions, three promising combustor concepts emerged: rich-burn quick-quench lean-burn (RQL) combustion, catalytic combustion, and lean-premixed (LPM) combustion, also known as lean-premixed prevaporized (LPP) combustion for liquid fuels [1]. The RQL technique had problems satisfying emissions requirements, especially in the areas of soot formation and incomplete mixing between fuel-rich combustion products and air. Catalytic combustion drawbacks included difficulties with cost, durability, and safety. Finally, LPM combustion appeared to have the most potential for application in practical systems, especially for applications where size and weight were not an issue such as power generation.

As the name suggests, lean-premixed combustion constitutes premixing the fuel and air upstream of the combustor and operating the combustor under fuel-lean conditions. The net outcome is reduced flame temperatures and severely decreased production of thermal $NO_x$ emissions [2]. Therefore, use of LPM combustion has had success in meeting the strict environmental emissions regulations of many developed nations. Despite such emissions reduction success, LPM combustors suffer from a particularly problematic drawback: an increased susceptibility to self-sustained combustion instabilities.

### 1.1.1 Combustion Instabilities

"Combustion instability" can be defined as persistent high amplitude pressure fluctuations resulting from the coupling of system acoustics and unsteady heat release. Originally observed and explained by Rayleigh [3], combustion instabilities have been encountered in numerous practical applications such as land-based gas turbines used for power generation, industrial burners, and afterburners. Their presence is undesirable because they decrease system efficiency and can bring about harsh vibrations and excessive heat transfer that damage engine components. Figure **1-1** juxtaposes a burner assembly damaged by combustion instability and a new burner assembly [4].

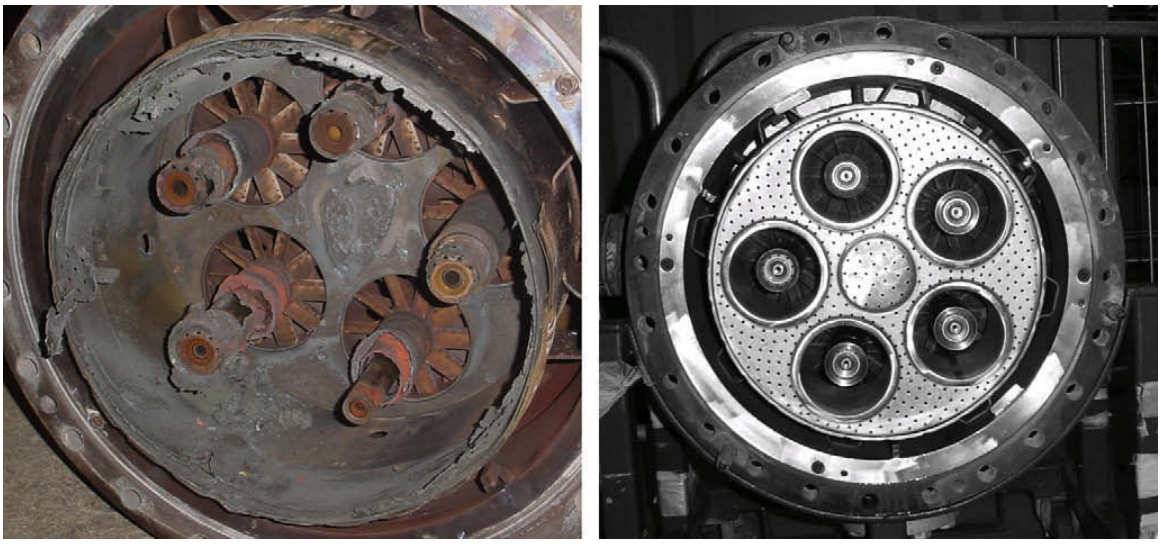

Figure **1-1**: Pictures of a burner assembly damaged by combustion instability (left) and new burner assembly (right) [4].

Combustion designers need a theoretical model with robust predictive capabilities to limit a combustor's exposure to combustion instabilities for operating conditions specified by design requirements. Otherwise, a combustor needs to be modified post-design stage to eliminate combustion instabilities. To obtain such a model, a thorough understanding of the physics of the phenomenon is necessary. Among the drivers of combustion instability, the two that play the

biggest role in inducing limit cycle oscillations are the formation and convection of coherent large-scale structures caused by large inlet velocity perturbations and equivalence ratio non-uniformities [5]. Therefore, the development of a theoretical model with such predictive capabilities requires understanding of the flame response to perturbations of inlet velocity and equivalence ratio.

### 1.2 Premixed Flame Response Review

A premixed flame when subjected to a velocity perturbation will react in the manner shown in Figure **1-2** [6]. Velocity perturbations disturb the flame's position, which directly affects its surface area. The direct influence of pressure, temperature, and density variations on the heat release rate is usually negligible for turbulent premixed flames [7]. Because premixed flames eliminate non-uniformities in equivalence ratio, the source of flame response can be attributed to the inlet velocity perturbation, assuming the flame is premixed upstream of a choked inlet to the combustor.

To quantitatively describe a flame's response to upstream velocity perturbations, a flame transfer function (FTF) describing the ratio of normalized heat release rate and normalized inlet velocity fluctuation is employed:

$$FTF(f, A) = \frac{Q'(f)/\overline{Q}}{V'(f)/\overline{V}} \qquad (1)$$

$$Gain \equiv \left|FTF\right| \qquad (2)$$

where $\overline{Q}$ is the time-averaged heat release rate, $\overline{V}$ is the mean velocity of the mixture in the mixing section, $Q'(f)$ and $V'(f)$ are their corresponding amplitudes at the forcing frequency, $f$, and $A$ is the magnitude of $V'(f)/\overline{V}$. The flame transfer function can be obtained from

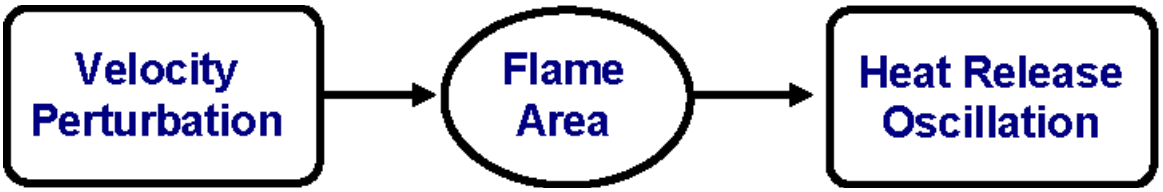


Figure **1-2** Dominant process for the generation of heat release oscillations originating from acoustic velocity perturbations [6].

experimental [8-11], numerical [12-13], and theoretical [14-18] based methods. Experimental methods capture the complex interactions inherent in combustion instabilities and are often used to validate results obtained by the other methods. Once obtained, the flame transfer function can be incorporated into a thermo-acoustic network model as a source term to predict combustion instabilities [19-20].

Flame transfer functions for laminar premixed flames have been well studied [16,18,21]. Fleifel et al. [18] analytically described the response of a laminar premixed flame to flow oscillations and concluded the flame transfer function was primarily governed by the flame Strouhal number, defined as $\omega R/S_L$. Lieuwen [21] reported that the flame transfer function of premixed flames was strongly dependent upon three parameters: a Strouhal number, $St = \omega L_f/u_o$, the ratio of the flame length to width, $\beta = L_f/R$, and the flame shape (i.e., conical, inverted wedge, etc.). Similar to results of analytic and experimental investigations of laminar flame transfer functions, Kim et al. [22] experimentally determined that the dynamics of turbulent premixed flames is governed by three parameters: the Strouhal number, $St = L_{flame}/L_{conv}$, the flame length $L_{flame}$, and the flame angle, $\alpha$, where the flame length and angle are defined relative to the location of maximum heat release. Qualitatively, the dynamics of turbulent and laminar flames remain similar [23].

Analytical and experimental works show that flame transfer function gain decreases as the velocity perturbation amplitude is increased. Often, for a given perturbation frequency, the

gain is constant with increasing velocity forcing amplitude, meaning the heat release response and input velocity fluctuation have a linear relationship, until a certain perturbation amplitude is reached. Then, the flame transfer function gain begins to decrease with increasing forcing amplitude. These two flame response regimes are often referred to as the linear and nonlinear response regimes [21,24].

In general, the global flame behaves as a low pass filter [8,21]. Schuller et al. [16] analytically examined laminar flame transfer function behavior for conical and V-flame shapes. While the global response was that of a low pass filter, the V-flame was also found to behave as an amplifier for a certain range of frequencies. There was no mention, however, that flame response mechanisms occurring on a local, rather than global, scale could disrupt this preferred frequency amplifier and global low pass filter behavior.

### 1.3 Premixed Flame Response Mechanisms

Two flame response mechanisms primarily govern flame dynamics for premixed flames subjected to upstream velocity oscillations: perturbations resulting from flow non-uniformities caused by vorticity disturbances or perturbations that propagate along the flame surface and originate from the flame anchoring point [14]. Durox et al. [10] explains the flame response mechanism due to flow non-uniformities. Although the study was conducted on bluff-body stabilized inverted conical flames, the description is still relevant for bluff-body stabilized "V" flames. Figure **1-3** presents axial velocity profiles [10]. The top profile represents the mean velocity for an unforced flame and two levels of velocity forcing and the bottom profile represents the rms fluctuation in velocity for the same forcing conditions. In the presence of excitation, the velocity fluctuation is not uniform. Velocity perturbations are enhanced along the edges, in the highly sheared oscillating flow. Such flow non-uniformities can generate vorticity.

Three vortex kernels can be seen in the particle imaging velocimetry (PIV) results presented in Figure **1-4**. They are created at the burner exit in the shear layer separating the reactive jet from the surrounding air and are convected downstream along mean flow streamlines starting from the burner edge. In Figure **1-4**, the vortex kernels can be observed impinging on the flame.

The other premixed flame response mechanism works similar to a string attached at one end and allowed to freely vibrate at the other. Flame perturbations originate at the flame anchoring point and propagate along the flame surface. It is the propagation of these perturbations that disturbs the flame's surface area, thus disturbing the flame's heat release. Chadhuri et al. [25] investigated spatial mixture gradients of bluff-body stabilized conical premixed turbulent flames. In that study, they presented observations of the two premixed flame

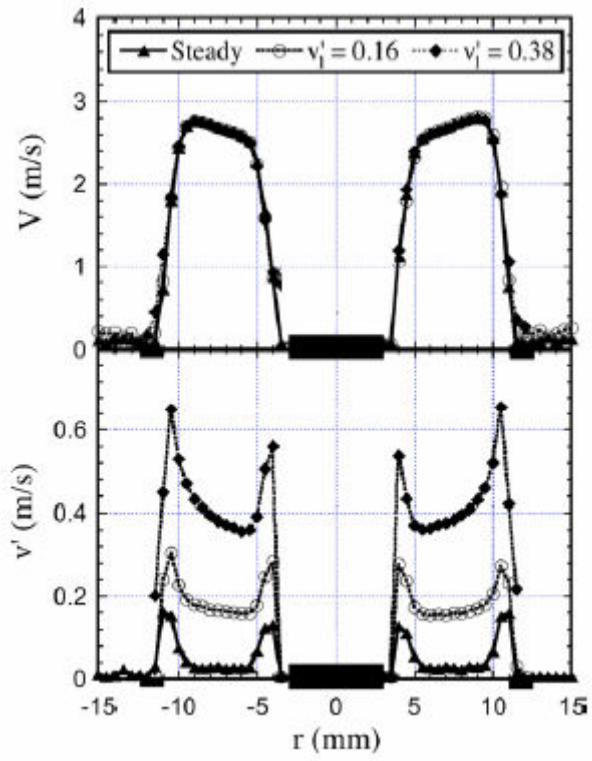


Figure **1-3**: Axial velocity profiles of mean velocity, V, (top) and rms velocity fluctuation, v', (bottom). Operating conditions: $V_{mean}$ = 2.05 m/s, $\Phi$ = 0.92, f = 100 Hz [10].

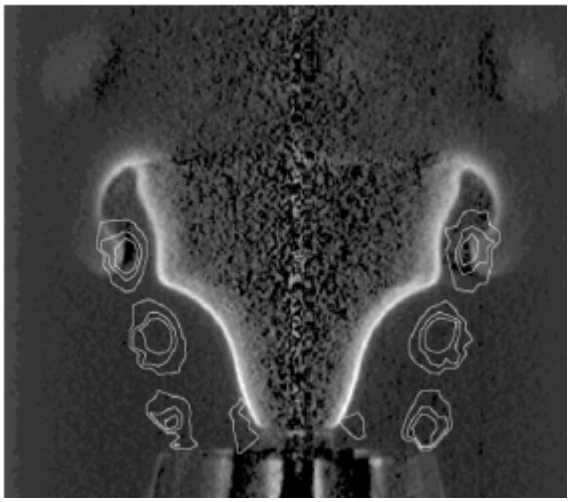

Figure **1-4**: Unsteady vorticity field and flame front location at one instant in the cycle. The flame position is obtained by applying an Abel transformation to the instantaneous emission image. Operating conditions: $V_{mean}$ = 1.87 m/s, $\Phi$ = 0.8, rms velocity = 0.15 m/s at r = 7 mm, f = 150 Hz [10].

response mechanisms in flames with uniformly premixed reactants. The flame root response mechanism can be observed propagating along the flame front near the base of the conical flame in the high speed CCD camera images (no spectral filtering) in Figure **1-5**. Also seen in the figure, the flame response mechanism due to flow non-uniformities is said to affect the flame wing structures near the top of the images. Chadhuri et al. [25] claim that the interaction of these two flame response mechanisms results in the large flame wing structure and strongly influence the global nature of the flame transfer functions. The study, however, is limited to conical flames and little detail is given to possible constructive or destructive interactions within the forcing period.

Preetham et al. [14] analytically described interactions between the two premixed flame response mechanisms for conical flames and wedge ("V") flames. They reported that flame dynamics were primarily governed by the two mechanisms, which produced waves that propagated along the flame sheet. Depending on the phase speed, the waves could interact

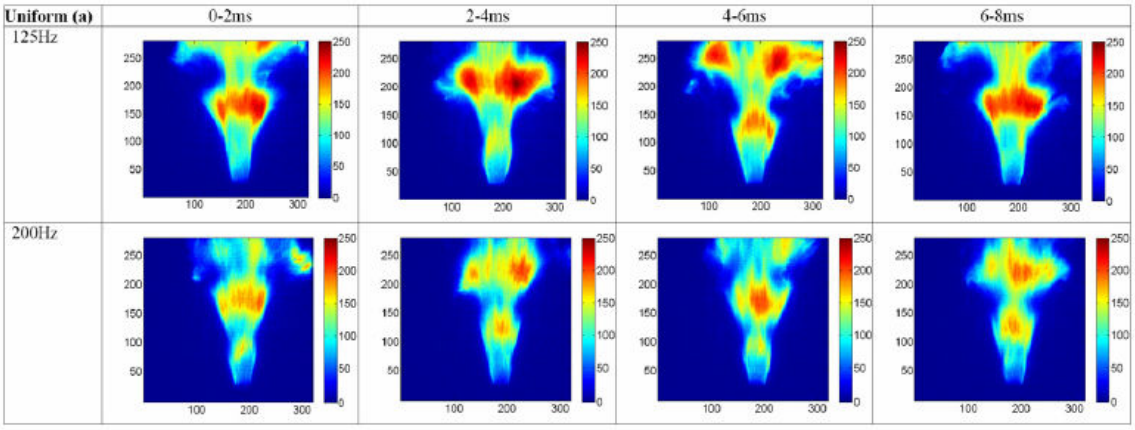


Figure **1-5**: High speed flame emission images (no spectral filtering) at 500 frames per second and 2 ms exposure. Operating conditions: $V_{mean}$ = 15 m/s, $V'/V_{mean}$ = 8%, f = 125 Hz and 200 Hz. [25].

constructively or destructively. A plot of flame transfer function gain due to velocity disturbances versus a reduced Strouhal number ($St_2$) is presented in Figure **1-6** for a "V" flame [14]. This "reduced Strouhal number" is a ratio of the Strouhal number (St) and the ratio of the flame length to the flame radius (β):

$$St_2 = \frac{St}{\alpha} \qquad (3)$$

where $St = \frac{\omega_0 L_F}{u_0}$, $\beta = \frac{L_F}{R}$, $\alpha = \frac{\beta^2}{\beta^2 + 1}$

$\omega_0$ is angular frequency, $L_F$ is flame length, $u_0$ is mean flow velocity, and R is flame radius. The parameter η in the figure refers to the phase speed of the velocity disturbance. For a sense of scale, η=0 refers to the case of a uniform disturbance velocity and η=1 refers to the case when the velocity disturbance phase speed is equal to the flame front disturbance velocity (mean flow velocity). The phase speed of the disturbance is less than the mean flow speed for η>1 and greater than the mean flow speed for η<1. Referring back to Figure **1-6**, for any η not equal to 1 or 0, the gain increases to values greater than unity when the two flame response mechanisms

interact constructively. Similarly, the flame response mechanisms interact destructively at Strouhal numbers where the gain is zero.

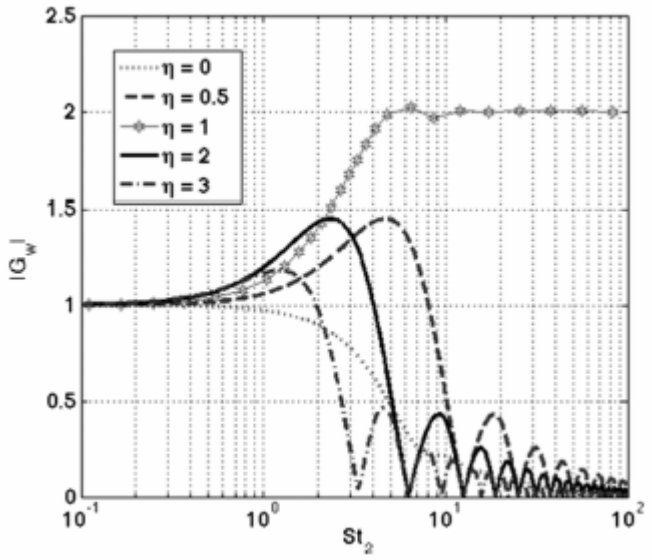


Figure **1-6**: Axisymmetric wedge flame transfer function gain versus reduced Strouhal number $St_2$ for different values of η (a parameter describing disturbance velocity) [14].

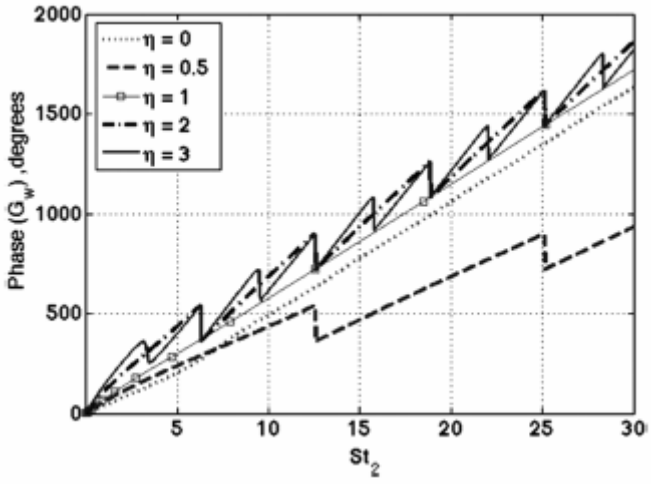


Figure **1-7**: Axisymmetric wedge flame transfer function phase versus reduced Strouhal number $St_2$ for different values of η (a parameter describing disturbance velocity) [14].

Phase characteristics are presented in Figure **1-7** [14]. The phase increases with reduced Strouhal number with similar characteristics for all η values. At Strouhal numbers of zero gain, the phase encounters a phase discontinuity of -180°.

Preetham et al. [14] also investigated the effect of velocity forcing amplitude on flame response. Figure **1-8** shows flame transfer function gain versus a reduced Strouhal number and a parameter ε normalized by $\varepsilon_f$. The parameter ε in this case represents the normalized velocity perturbation $V'/V_{mean}$ and $\varepsilon_f$ represents the velocity forcing amplitude where flame flashback occurs. As the velocity amplitude is increased, i.e. as $\varepsilon/\varepsilon_f$ is increased, the individual gain due to each of the two flame response mechanisms decreases. Since the relative "ages" of the two disturbances is unequal, however, the magnitude of their gain reduction is different. With increased forcing amplitude, the Strouhal number of minimum gain shifts to a higher value. So, for a given $St_2$ with a flame transfer function gain of zero, increasing the velocity forcing amplitude would yield a non-zero gain. At higher velocity disturbance amplitudes, the interaction of the two mechanisms do not exactly cancel and the gain does not go to zero.

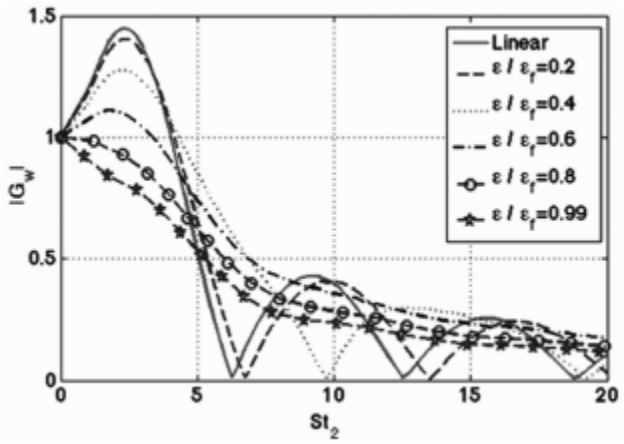


Figure **1-8**: Dependence of velocity forcing amplitude for axisymmetric wedge flame transfer function gain versus Strouhal number, η = 2 [14].

### 1.4 Research Objectives and Approach

The flame transfer function will be experimentally determined. A siren modulation device will impose velocity perturbations on the premixed fuel and air and photomultiplier tubes will record chemiluminescence intensity, an indicator of the heat release rate. One objective will be to observe the premixed flame response mechanisms and their possible interaction. To do this, chemiluminescence images of the overall flame structure will be recorded with an ICCD camera. Images will also be phase synchronized with the inlet velocity perturbation to provide flame dynamics information within a forcing period. In addition to taking fixed velocity forcing amplitude chemiluminescence intensity measurements and chemiluminescence images, the effect of velocity forcing amplitude on the interaction of the flame response mechanisms will be investigated by varying the inlet velocity forcing amplitude at a fixed forcing frequency.

## Chapter 2

# Experimental Methods

### 2.1 Experimental Setup

To investigate the response of the premixed flame heat release rate to velocity fluctuation, an experimental rig was designed such that velocity perturbations are the only source of disturbance to the flame. Fluctuations in equivalence ratio are eliminated by ensuring the inlet mixture of fuel and air is entirely premixed before encountering a choked orifice. Therefore, flow oscillations generated downstream of the choked orifice cannot propagate upstream and affect the mixing of fuel and air.

Premixed fuel and air pass through a siren modulation device before entering a plenum located immediately upstream of the injector. As shown in Figure **2-1**, a bypass line is utilized to control the amplitude of the modulation of the fuel-air mixture. The injector houses an axial swirler and a centerbody, which both assist in flame stabilization. At the exit of the injector, the fuel-air mixture enters a quartz tube combustor. The exit of the combustor is open and the exhaust flows into an exhaust hood. The combustor exit is open to reduce the possibility of self excited instabilities. Individual subsystems shown in Figure **2-1** are described in detail in the following sections: the air and fuel delivery system, siren, and combustor.

#### 2.1.1 Air and Fuel Delivery System

The air and fuel delivery system can be seen schematically in Figure **2-2**. Air is first pressurized by a compressor to 300 psi. Then, a de-humidifier removes moisture from the air. A

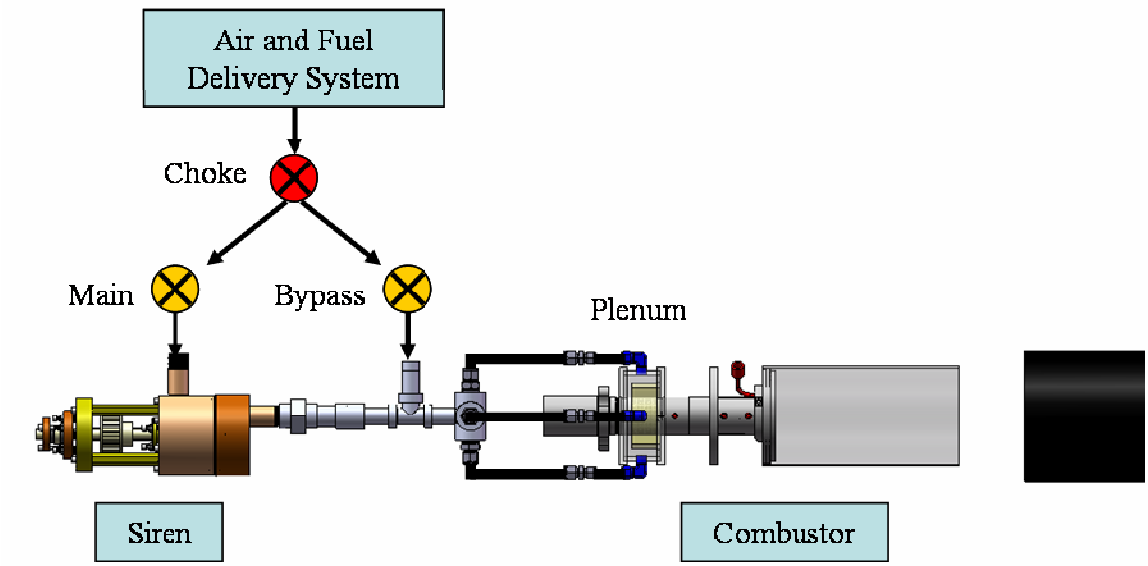


Figure **2-1**: Experimental setup schematic. Air and fuel are premixed upstream of the choke.

series of filters removes any compressor oil that may have been added in the process of pressurization. A dome regulator reduces the pressure to a set value of 150 psi. Next, the air passes through a flowmeter, which monitors the flowrate. Adjustment of a metering valve provides control of the air flowrate. Finally, the air enters a tee through which natural gas is introduced.

Figure **2-2** also illustrates the natural gas delivery system. Pressurized bottles house the natural gas (96% methane) fuel supply. Two consecutive pressure regulators decrease the pressure of the high pressure natural gas, which when the bottles are full is approximately 2700 psi, to 1700 psi and again to 200 psi. The fuel then travels through a flowmeter, the flowrate controlled by a metering valve. From there, fuel is introduced into the air stream perpendicular to the direction of air flow at a tee.

The fuel and air mix over a length of 10 feet through a tube diameter of 0.75”, ensuring that the mixture is fully premixed. To prevent downstream flow oscillations from affecting the

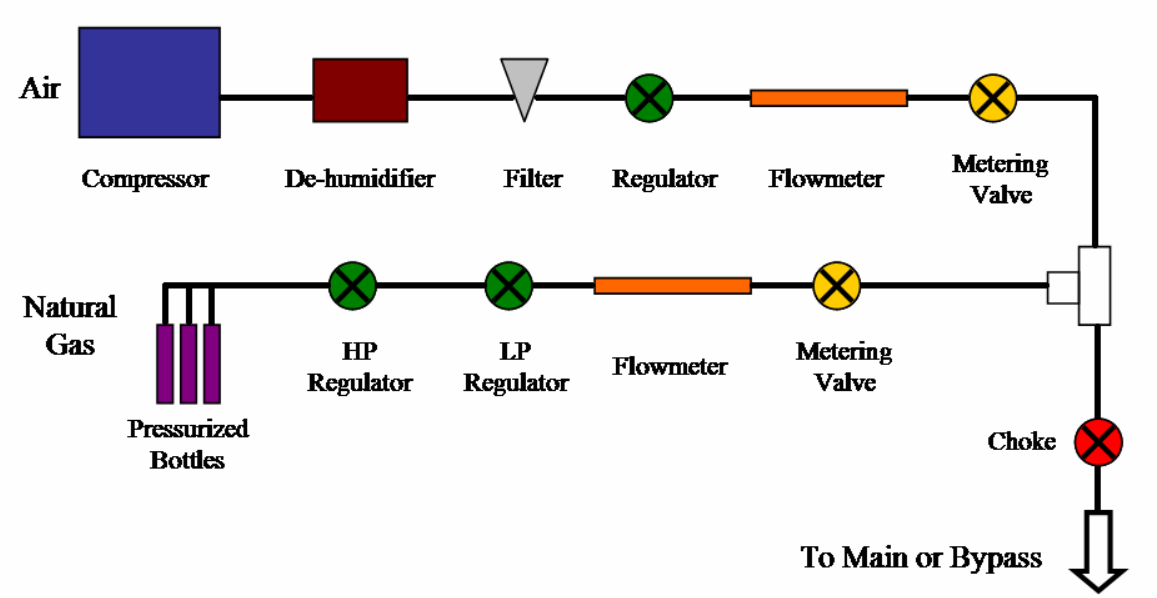


Figure **2-2**: Schematic drawing of the air and fuel delivery system.

mixing process, a choked orifice is placed at the end of the 10 foot long mixing tube. After the choked orifice, the fuel-air mixture flows to the siren.

### 2.1.2 Siren

A siren modulation device imposes inlet velocity perturbations. The siren is driven by a variable-speed DC brushless motor with a maximum speed of 5000 RPM. A timing belt connects the motor shaft to the siren shaft with a gear ratio of 2:1, thus the maximum speed of the siren shaft is 10,000 RPM. The siren and DC motor assembly is shown in Figure **2-3**. Attached to the siren's shaft is a rotor with 4 holes, seen in Figure **2-3** (right). Flush mounted with the rotor is a stator with a single hole. The fuel-air mixture flows through the siren when the hole in the stator and one of the holes in the rotor are aligned. The result is a modulation in the flow of the fuel-air mixture at frequencies between 30 and 500 Hz. The amplitude of the fuel-air modulation is adjusted by varying the amount of fuel-air mixture that bypasses the siren.

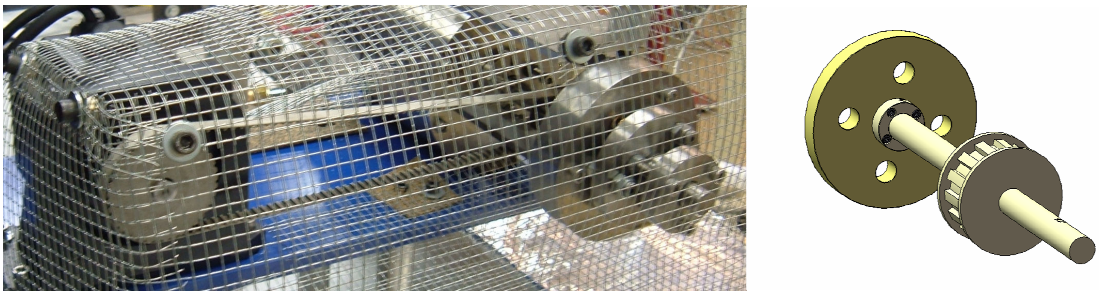

Figure **2-3**: Picture of DC motor, DC motor sprocket, timing belt, and siren under a wire mesh safety enclosure (left) and schematic of siren sprocket, shaft, and rotor (right).

### 2.1.3 Combustor

The combustor nozzle assembly is the same as the one utilized in Kim et al. [26]. The annular mixing section consists of a 60 mm I.D. mixing tube and a 40 mm O.D. centerbody, recessed 20 mm from the dump plane as shown schematically in Figure **2-4**. Within the mixing section, swirl vanes are mounted 120 mm upstream of the combustor dump plane. A port for a

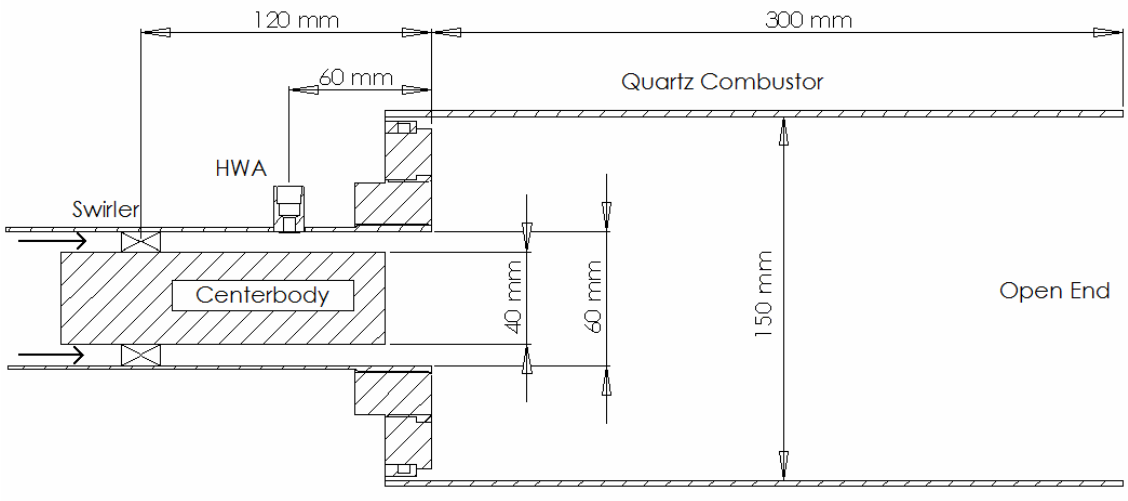


Figure **2-4**: Schematic drawing of mixing section and combustor. Dimensions in millimeters.

hot wire anemometer sits 60 mm upstream of the combustor dump plane. The optically accessible combustor consists of a fully open quartz tube (150 mm in diameter and 300 mm in length). To de-couple the acoustics of the exhaust and the combustor, the exhaust duct is set 150 mm downstream of the exit of the quartz tube. The separation can be seen in Figure **2-1**.

## 2.2 Test Conditions

Experiments were performed at atmospheric pressure and temperature (at the combustor inlet). Mean velocities in the nozzle were 20 m/s, 25 m/s, and 30 m/s with mean equivalence ratios (Φ) ranging from 0.65 to 0.80. The Reynolds number ranged from 23,700 ~ 35,600. Normalized inlet velocity forcing amplitudes, $V'/V_{mean}$, up to 35% were achieved depending on the forcing frequency. Fixed normalized inlet velocity forcing amplitudes up to 5% were achieved for a frequency range from 80 to 360 Hz. Experiment conditions are presented in Table **2-1**.

Table **2-1**: Experimental operating conditions.

| Parameters | Values |
|---|---|
| Mean Inlet Pressure, $P_{mean}$ | 1 atm |
| Inlet Temperature, T | 20°C |
| Mean Inlet Velocity, $V_{mean}$ | 20 m/s 25 m/s, 30 m/s |
| Mean Equivalence Ratio, Φ | 0.65, 0.70, 0.75, 0.80 |
| Forcing Frequency, f | 80 – 360 Hz |
| Normalized Forcing Amplitude, $V'/V_{mean}$ | Up to 35% |

## 2.3 Experimental Measurement Techniques

### 2.3.1 Dynamic Pressure

A high frequency, piezoelectric pressure transducer (PCB 112A04) measures combustor pressure fluctuations. The pressure transducer, mounted in a water-cooled adapter, sits at the end of a ¼" diameter tube which is flush mounted with the dump plane to obtain dynamic pressure measurements in the high temperature combustor environment. From the pressure transducer, the charge output is amplified and converted to a voltage signal by an in-line charge amplifier. The pressure signal is then conditioned by an amplifier, digitized, and stored in a computer. Dynamic combustor pressure measurements are used to in determine the presence of self-excited combustion instabilities. It is essential that there are no self-excited instabilities when flame transfer function measurements are made.

### 2.3.2 Velocity

Velocity measurements are an integral part of the flame transfer function measurements. A hot wire anemometer (HWA, TSI model 1210) measures the gas velocity in the annular mixing section 60mm upstream from the dump plane, as shown in Figure **2-4**. In order to convert the measured voltage signal into units of velocity, a calibration is necessary. Figure **2-5** presents an example of such a calibration curve. Voltages are recorded at points of known mean velocities. Then, a $2^{nd}$ order polynomial is fitted to these points. Substituting voltage data into the calibration polynomial allows conversion of the hot wire voltage signal into units of velocity.

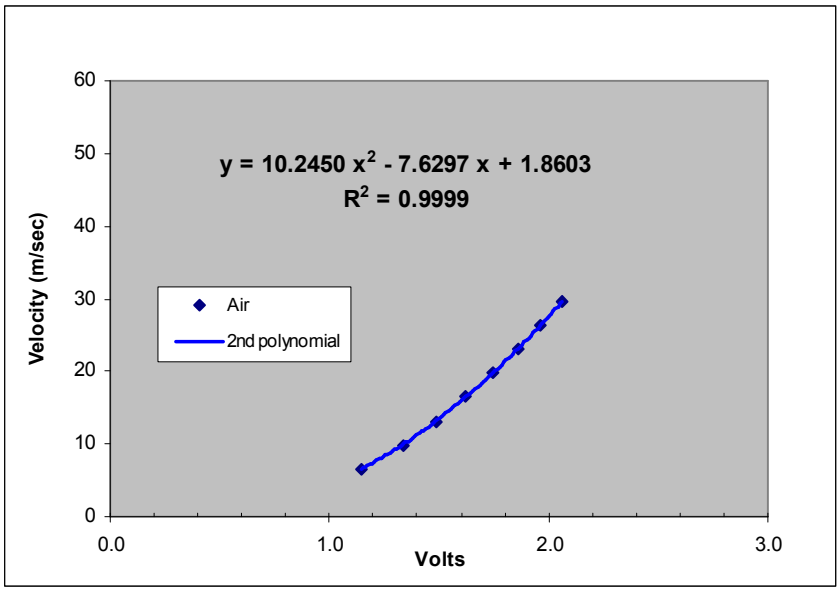


Figure **2-5**: Example calibration curve. The vertical axis represents velocity in units of m/s and the horizontal axis represents background-subtracted hot wire signal voltage.

One concern when using hot wire anemometry is the instrument's sensitivity to position and orientation. Each time the hot wire is moved, a new calibration curve must be obtained. To ensure the hot wire captured the velocity fluctuation of the flow accurately, the hot wire is positioned in the center of the flow passage so as to be outside the boundary layers.

A study was conducted to measure the mean hot wire signal at various positions and orientations. The hot wire was placed in five different locations between the inner diameter of the mixing section tube (position 1 shown in Figure **2-6**) and the outer diameter of the centerbody (position 5) in 1/16" increments. In addition, the hot wire was placed at two different orientations with respect to the mean flow direction, i.e., 90° and 0°. For the same constant flowrate of air, the 90° orientation provided more signal response than the 0°. Positions 3 and 4 yielded the greatest hot wire signal response for the 90° orientation, Figure **2-7**. Although the hot wire's most important role is measuring the flow velocity fluctuation, the mean velocity must be known to calculate the velocity fluctuation. Therefore, picking a hot wire measurement location that

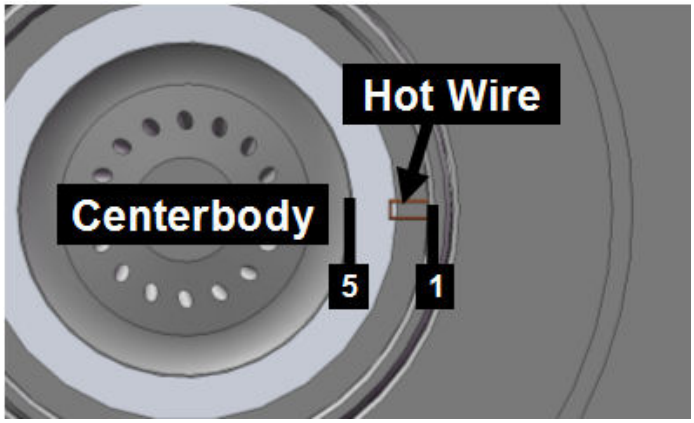


Figure **2-6**: Schematic of hot wire locations starting at position 1, the inner diameter of the burner tube, and ending at position 5, a position very near the outer diameter of the centerbody. Each numbered position represents a move of 1/16". The hot wire shown in the figure is positioned 90° with respect to the horizontal.

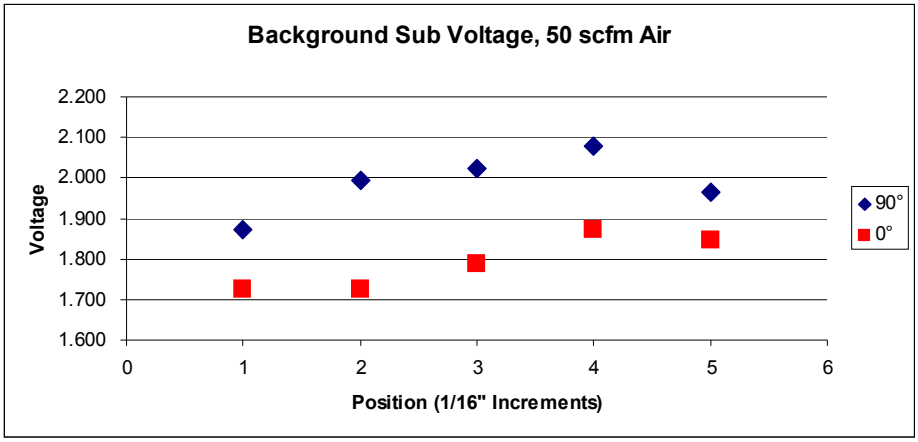


Figure **2-7**: Constant air flowrate comparison of hot wire signal response for different positions and orientations. Background subtracted voltage is presented for 90° and 0° orientations.

provides accurate mean velocity results is important. The hot wire location and orientation used for flame transfer function measurements was between positions 3 and 4 with a 90° orientation.

Other parameters possibly affecting the hot wire measurement include mixture composition, presence of the flame, forcing frequency, and forcing amplitude. To investigate the effects of mixture composition, the hot wire calibration curves for pure air and premixed fuel and air (mean equivalence ratio 0.70) were compared. Since natural gas has different properties than

air and the hot wire measurement is based on convection heat transfer, the addition of natural gas could affect the hot wire reading. The quantity of natural gas for the equivalence ratios of interest, however, was so low when compared to the quantity of air that the addition of natural gas did not affect the hot wire signal, as shown in Figure **2-8**.

The presence of a flame can also affect the hot wire signal as a result of radiative heat transfer from the hot combustion gases. A calibration curve with combustion (at mean equivalence ratio 0.70) is juxtaposed with cold flow premixed fuel and air (also at Φ=0.70) in Figure **2-8**. The net result is that an insignificant amount of heat is transferred upstream when combustion takes place, and the calibration curve obtained for air under cold flow conditions can be applied to experimental operating conditions. In the interest of practicality, velocities for flame transfer function measurements presented in later sections are obtained from cold flow air calibration curves.

The effects of forcing frequency and amplitude on the mean hot wire signal are also investigated and found to be negligible, as shown in Figure **2-9**. For a range of forcing

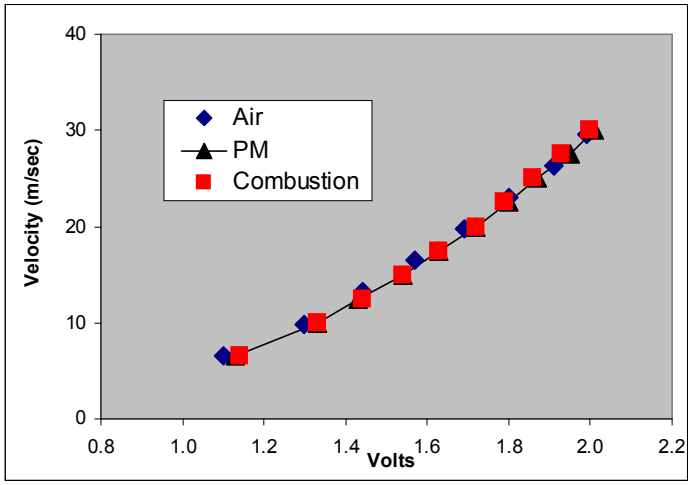


Figure **2-8**: Hot wire calibration curves obtained for cold flow air (Air), premixed fuel and air Φ = 0.70 cold flow (PM), and premixed fuel and air Φ = 0.70 with combustion (Combustion).

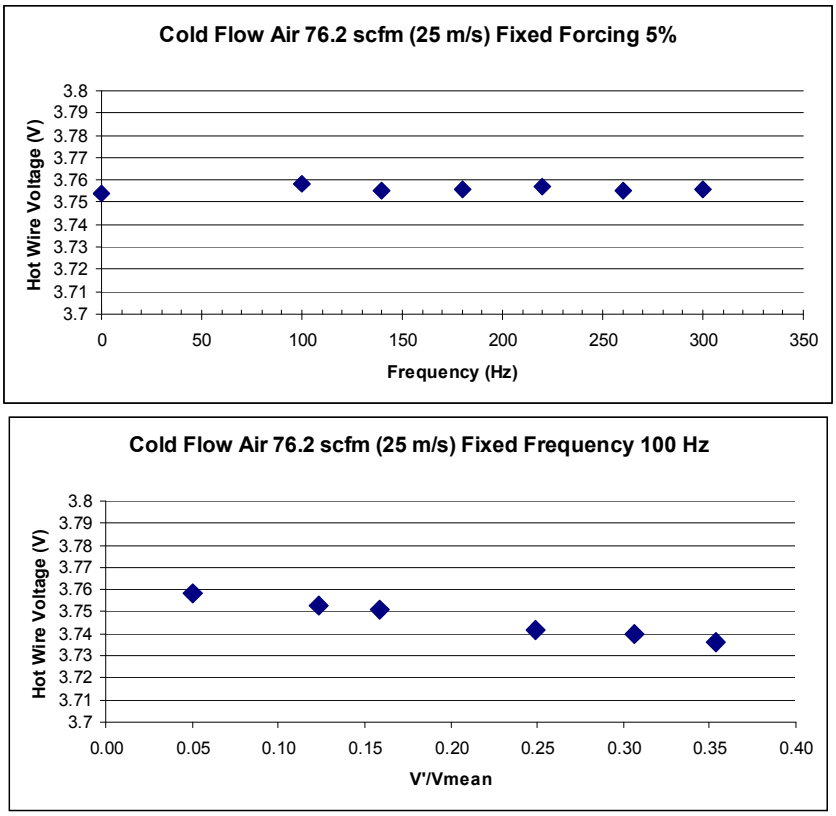


Figure **2-9**: Mean hot wire response for constant cold flow air at variable forcing frequencies under fixed inlet velocity harmonic forcing amplitude $V'/V_{mean}$ = 5% (top) and variable inlet velocity harmonic forcing amplitudes under fixed forcing frequency 100 Hz (bottom).

frequencies at constant forcing amplitude, the mean hot wire signal varies less than 1%. For the range of forcing amplitudes, up to the maximum obtainable by the siren modulation device, at a constant forcing frequency; the mean hot wire signal also varies less than 1%.

### 2.3.3 Total Chemiluminescence Intensity

In addition to velocity, a measure of heat release rate is required to calculate the flame transfer function. Chemiluminescence intensity has been used extensively in combustion instability studies as an indicator of heat release rate [5]. The justification for this is based on the experimental observation that the overall chemiluminescence intensity increases linearly with

increased fuel flow for a fixed equivalence ratio, where the slope increases with increasing equivalence ratio [5]. Three photomultiplier tubes (PMT, Hamamatsu model H7732-10) were used to measure global chemiluminescence emission intensity. They were installed outside the quartz combustor with full optical view of the entire reaction region. Figure **2-10** provides a typical chemiluminescence emission spectrum for a lean premixed gas turbine combustor [27]. The chemiluminescence emissions from CH* and OH* occurs over a narrow wavelength interval and $CO_2$* chemiluminescence occurs over a very broad range of wavelengths. To isolate emission data from the three species, a narrow band-pass filter is mounted in each of the three PMTs. The filters are selected to facilitate the measurement of global CH* (432 ± 5 nm), $CO_2$* (365 ± 5nm), or OH* (307 ± 5m). Appendix **A,** Figures **A-1** – **A-4**, provide PMT calibration information. CH* and OH* measurements yield similar results.

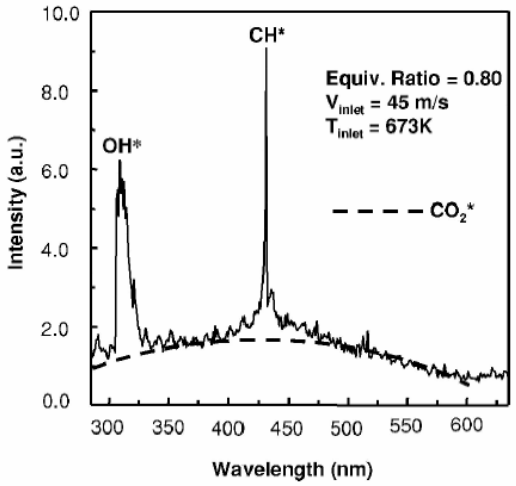


Figure **2-10**: Typical chemiluminescence emission spectrum of lean gas turbine combustor. Operating conditions: $P_{mean}$ = 100kPa, $V_{mean}$ = 45 m/s, Φ = 0.80, T = 673K [27].

### 2.3.4 CH* Chemiluminescence Images

Time-averaged CH* chemiluminescence images provide an overall understanding of the flame structure. An ICCD camera (Princeton Instruments model 576G) equipped with a CH* bandpass filter (430 ± 5mm) records line-of-sight (LOS) images of the axisymmetric flame. Within the image, chemiluminescence intensity is mapped to a pseudo color display. White-red represents maximum intensity and blue-black represents minimum intensity.

The CH* chemiluminescence images can be placed into three categories: unforced, forcing period averaged, and phase-synchronized with inlet velocity. Unforced images are the averaged results of 40 individual accumulations. The camera gain was set to 4.5 and the exposure time was set to 12.5 ms. Figure **2-11** shows a direct luminosity photograph (top) and a CH* chemiluminescence image displayed in pseudo-color (bottom), for the same operating condition.

Forcing period averaged CH* chemiluminescence images consist of images taken under forced velocity conditions, where the exposure time is set to one period of the forcing frequency. Images are taken for a range of forcing frequencies from 80 Hz to 350 Hz. Similar to the unforced images, the gain is set to 4.5 and 40 accumulations are averaged.

The final category of images, images taken under forced conditions and synchronized in phase with the inlet velocity perturbation, provides insight into flame structure within a forcing period. The phase-synchronized images are obtained by synchronizing the image acquisition with the hot wire signal. Camera gain is set to 9.5, 40-50 accumulations are averaged, and the gate width is set, depending on the overall flame intensity, from 40 μs to 240 μs. Images are recorded in phase intervals of 30°, resulting in a 12 image sequence.

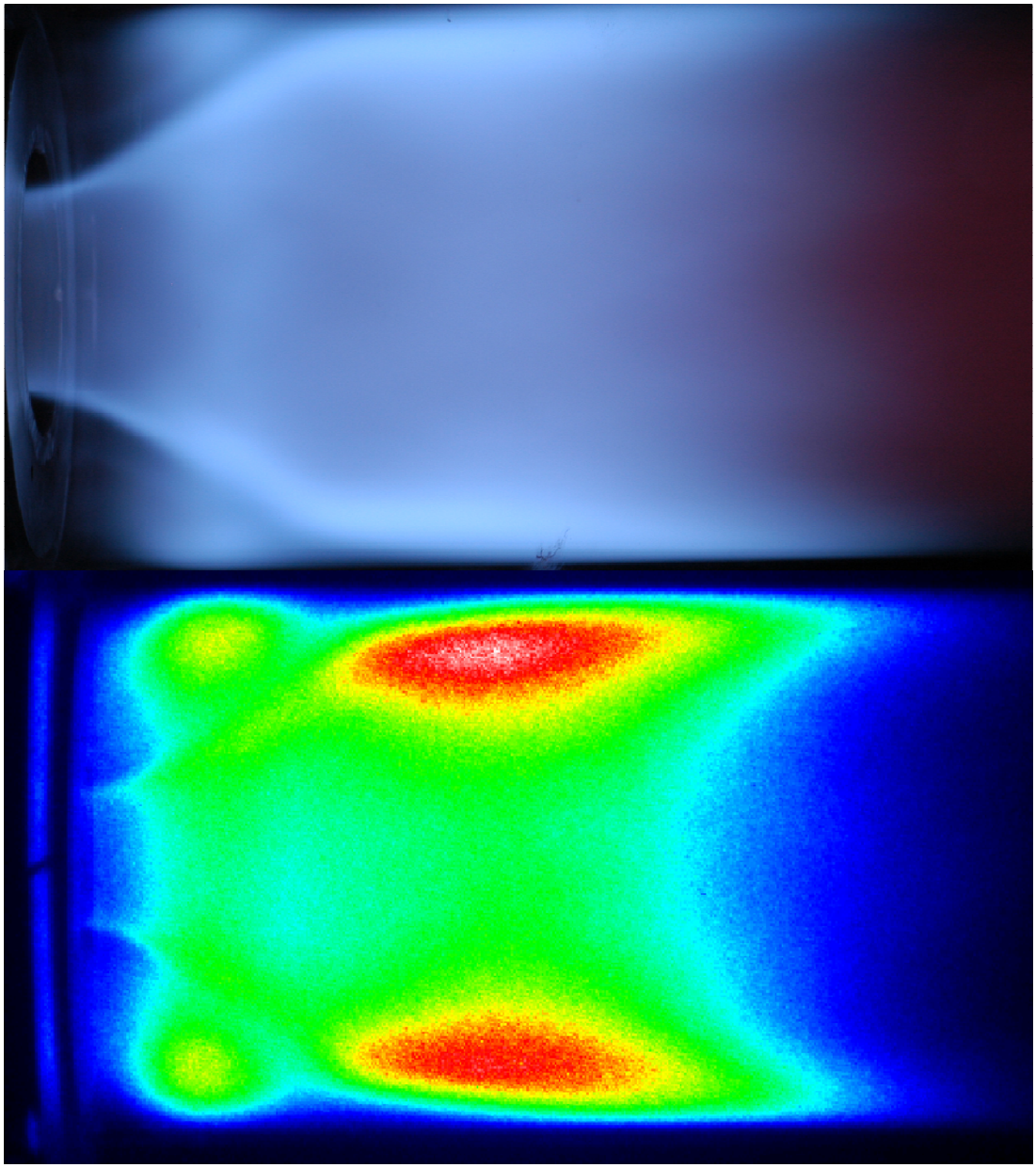

Figure **2-11**: Line-of-Sight (LOS) direct luminosity photo of unforced flame (top) and CH* chemiluminescence image (bottom) seen through quartz combustor. Operating condition: $V_{mean}$ = 30 m/s, $\Phi$ = 0.65.

## 2.4 Data Analysis and Processing

### 2.4.1 Data Acquisition and Frequency Domain Transformation

To acquire hot wire anemometer and PMT signal data, a digital data acquisition system recorded 32768 data points at a sampling rate of 8192 Hz for each test. Four seconds of time discrete time domain data was acquired and transformed into its frequency domain representation by means of a fast Fourier Transform (FFT). Figure **2-12** provides an example of CH* chemiluminescence time domain data for a forced velocity condition. Figure **2-13** displays the frequency spectrum obtained by applying an FFT to the same data set used in Figure **2-12**. From the frequency domain data, the amplitude is taken at the forcing frequency. Often, the amplitude is normalized by the mean and the ratio is presented such as in Figure **2-13**.

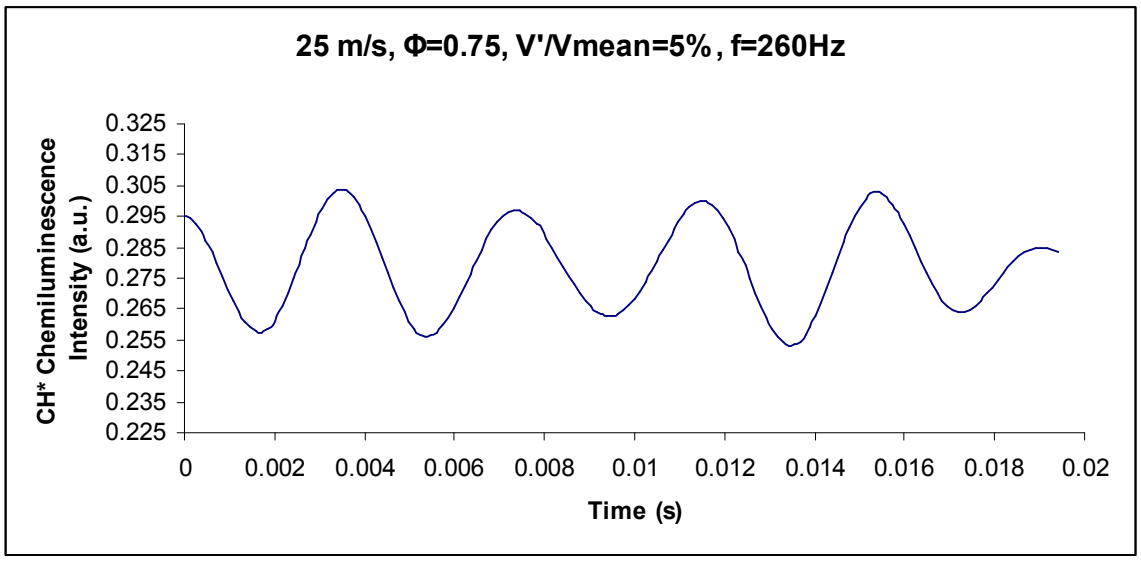


Figure **2-12**: CH* chemiluminescence signal (a.u.) versus time. Operating conditions: 25 m/s, $\Phi = 0.75$, $V'/V_{mean} = 5\%$, forcing frequency = 260 Hz.

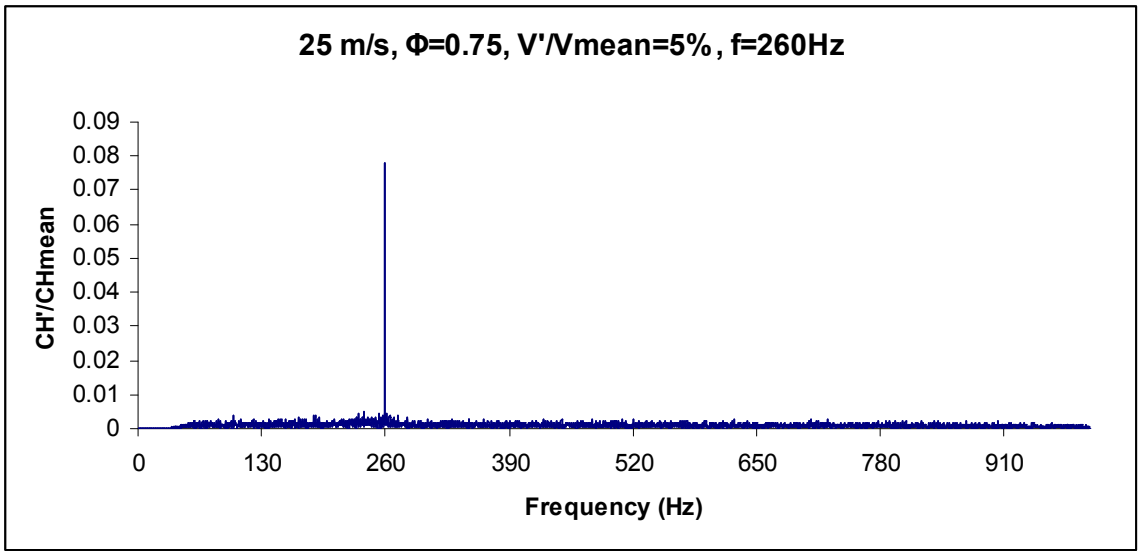


Figure **2-13**: Normalized frequency spectrum of CH* chemiluminescence signal. Operating conditions: 25 m/s, $\Phi = 0.75$, $V'/V_{mean} = 5\%$, forcing frequency = 260 Hz.

### 2.4.2 Chemiluminescence Image Deconvolution

To extract the two-dimensional flame structure, a three point Abel deconvolution scheme was applied to the CH* chemiluminescence line-of-sight images [28]. Figure **2-14** shows an example of deconvoluted flame image for the same operating condition as the images presented in Figure **2-11**. Only the upper half of the flame is presented because the flame is axi-symmetric.

The spatial coordinates of the flame center of mass (COM) are obtained from the image processing program Winview by examining the image statistics. The COM is calculated based on the intensity-weighted position of each pixel. Brighter pixels exert a greater influence on the COM location than darker ones. To assign a relevant length to the flame, it is first necessary to define a spatial origin. The origin is defined as the top corner edge of the centerbody if it were not recessed from the dump plane. So, the origin exists at the dump plane with respect to a

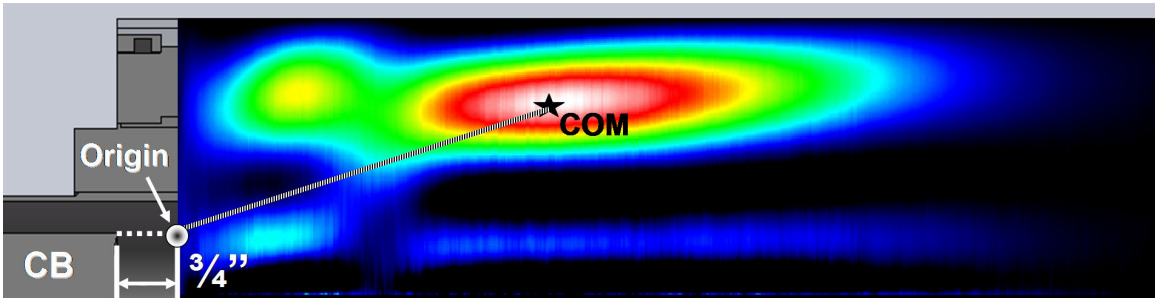


Figure **2-14**: Deconvoluted flame image shown with coordinates for flame center of mass (COM) and the origin as defined with respect to the experimental rig. The centerbody (CB) is recessed ¾”. Operating conditions: $V_{mean}$ = 30 m/s, $\Phi$ = 0.65.

horizontal axis and at the outer diameter edge of the centerbody with respect to a vertical axis, as shown in Figure **2-14**. The distance between the flame COM and the origin, defined as $L_{COM}$, represents the effective flame length or the convection flame length scale of a given flame.

# Chapter 3

# Results and Discussion

## 3.1 Unforced ICCD Camera Chemiluminescence Imaging

Previous results show that the gain and phase of the flame transfer function depend on flame structure (both flame shape and characteristic flame length) as well as the frequency and magnitude of inlet-velocity modulation [16,22,26,29]. In addition, flames with the same characteristic length exhibit very similar flame response regardless of their inlet flow conditions [22]. The flame length is found to be an important parameter determining flame response to inlet velocity perturbations. Therefore, unforced premixed flame structure is examined in this section.

Time-averaged CH* chemiluminescence images provide insight into the overall flame structure. Table **3-1** presents flame images for four equivalence ratios and three inlet velocities. The flow direction is left to right, and as described in the Section **2.4.2**, the flame images are deconvoluted. Only the upper halves of the deconvoluted images are shown because the reconstructed images are axisymmetric. To elucidate differences in intensity, the intensity of chemiluminescence is displayed in pseudo color with black representing the lowest intensity magnitudes and white representing the highest intensity magnitudes. Each image in Table **3-1** shows that the heat release is spatially distributed and a relatively high intensity region exists near the center of the flame. The intensity scales are unique to each image in order to provide insight into the relative high intensity region of each operating condition compared to the overall flame shape. If all the operating conditions of Table **3-1** were scaled to one intensity scale, images at operating conditions of an equivalence ratio of 0.65 would be significantly less visible compared to images at operating conditions with an equivalence ratio of 0.80. Also, the high intensity

Table **3-1**: Unforced deconvoluted flame images (CH* chemiluminescence). Operating conditions: $V_{mean}$ = 20 m/s, 25 m/s, 30 m/s and Φ = 0.65, 0.70, 0.75, 0.80.

| $V_{mean}$ \ Φ | 0.65 | 0.70 | 0.75 | 0.80 |
|---|---|---|---|---|
| 20 m/sec | 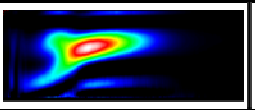 | 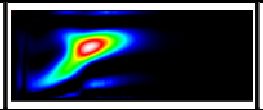 | 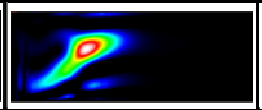 | 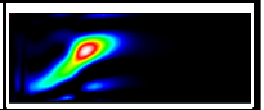 |
| 25 m/sec | 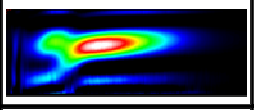 | 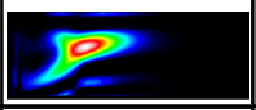 | 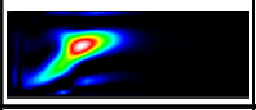 | 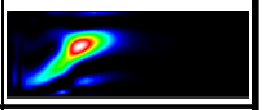 |
| 30 m/sec | 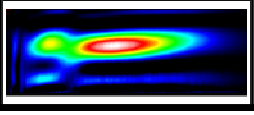 | 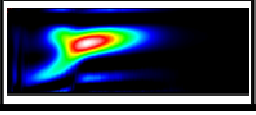 | 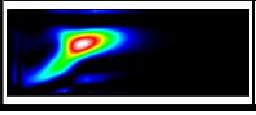 | 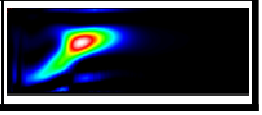 |

region corresponds to the existence of a highly wrinkled flame front, resulting in a greater flame surface area and thus a greater heat release. In the case of a premixed flame, an increase in flame surface area should be accompanied with an increase in heat release.

Two general flame shapes are observed in Table **3-1**: typical "V" flames (for example, $V_{mean}$ = 20 m/s and Φ = 0.80) and "V" flames with an extension into the outer corner recirculation zone (for example, $V_{mean}$ = 30 m/s and Φ = 0.65). To quantitatively describe flame shape, a flame center of mass (COM) is calculated from the flame image. The COM is calculated based on the intensity-weighted position of each pixel. Pixels with larger intensities exert a greater influence on the COM location than pixels with smaller intensities. As shown in Figure **3-1**, the distance between the flame COM and the top edge of the centerbody at the dump plane ($L_{COM}$) can be used to represent the overall flame length . The magnitude of $L_{COM}$ increases as inlet mean velocity is increased and decreases as mean equivalence ratio is increased. Shorter flame lengths, $L_{COM}$ < 80mm, typically exhibit a "V" flame shape, the first general flame shape observed in Table **3-1**. As flame length is increased, the flame extends into the outer corner recirculation zone and

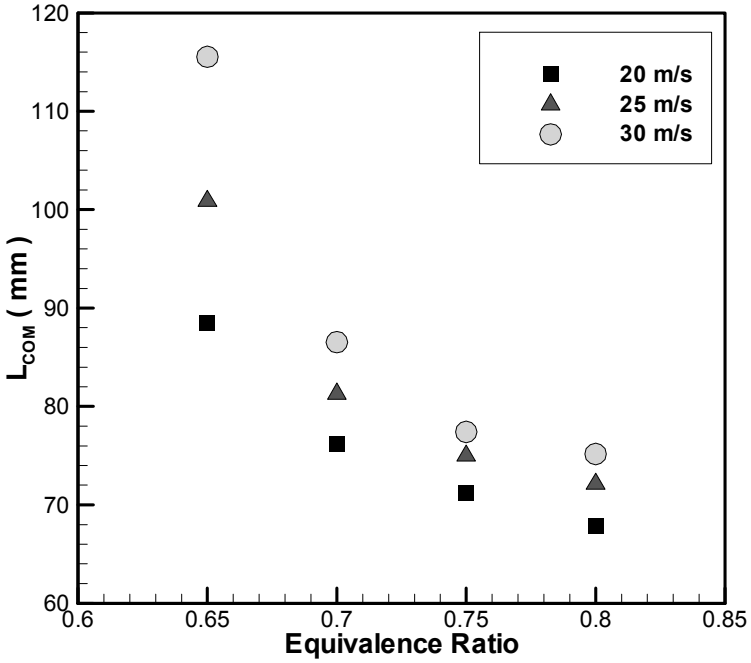


Figure **3-1**: Unforced flame length ($L_{COM}$) comparison for different mean equivalence ratios and velocities. Dimensions in millimeters. Operating conditions: $V_{mean}$ = 20 m/s, 25 m/s, 30 m/s and $\Phi$ = 0.65, 0.70, 0.75, 0.80.

resembles the second general flame shape observed in Table **3-1**, as seen in the condition 30 m/s, $\Phi$=0.65. Similar turbulent, swirl-stabilized flame structure results, including emergence of the flame into the outer corner recirculation zone, were found in previous studies [22,26].

Two approaches to obtaining a measurement of flame heat release rate from CH* chemiluminescence images are used. The first approach examines the mean flame surface area calculated from the flame image's line of maximum chemiluminescence intensity, along a radius at each axial location. In Figure **3-2a**, an example deconvoluted chemiluminescence image is portrayed with the line of maximum chemiluminescence intensity shown in black. The radial dimension from the centerline of the axisymmetric flame to the line of maximum intensity is defined as $r_m$.

(a)

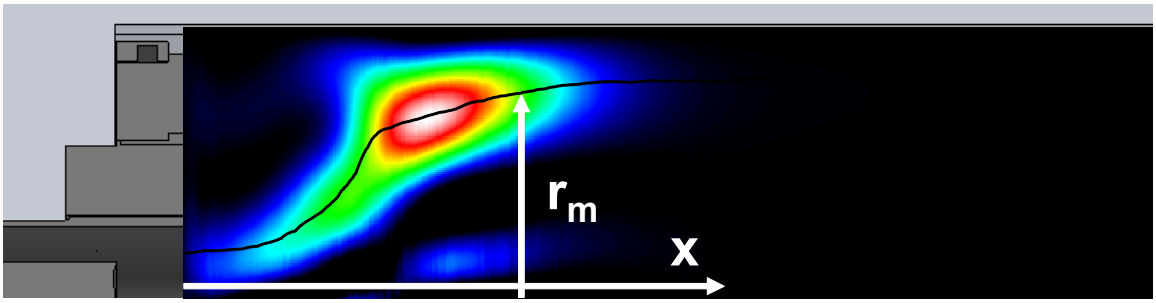


(b)

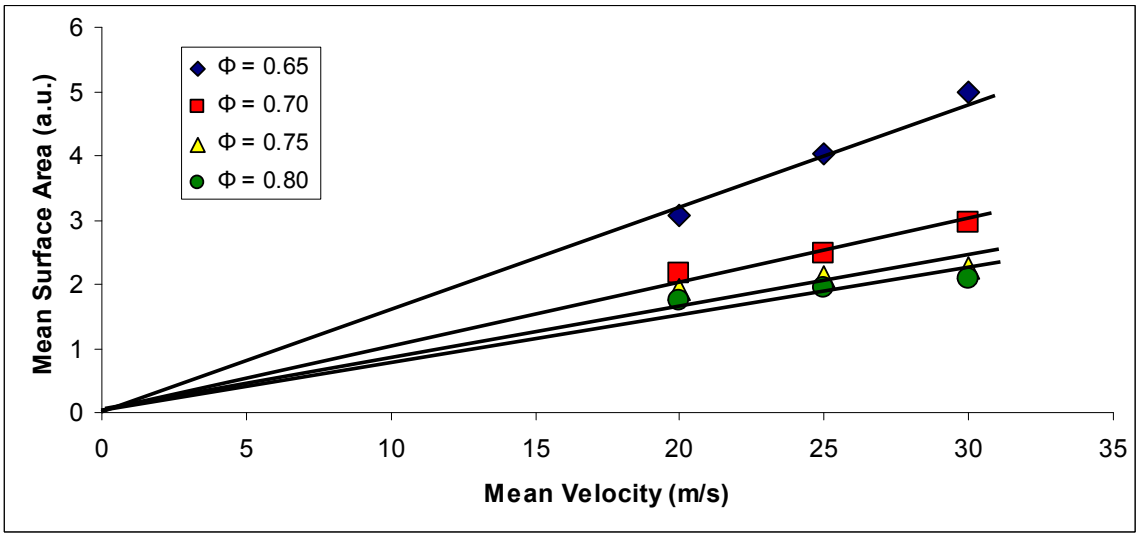


Figure **3-2**: (**a**) CH* deconvoluted chemiluminescence image illustrating the mean flame surface area measurement. Radial measurement $r_m$ begins at the combustor centerline and extends to the line of maximum intensity, shown in black. The variable $x$ represents axial distance measured from the combustor dump plane. Operating conditions: $V_{mean}$ = 25 m/s and Φ = 0.75. (**b**) Mean flame surface area (arbitrary units) comparison for unforced flames with different mean equivalence ratios and velocities. Operating conditions: $V_{mean}$ = 20 m/s, 25 m/s, 30 m/s and Φ = 0.65, 0.70, 0.75, 0.80.

The formula to calculate the mean flame surface area, $\bar{A}_s$ is:

$$\bar{A}_s = \int_0^L 2\pi r_m dx \qquad (4)$$

where L is the maximum axial, x direction, length of the line of maximum chemiluminescence intensity. This formula is then applied to the chemiluminescence image data with a MATLAB computer program. The details of this program can be broken down into a series of steps:

1) The chemiluminescence images, which are comprised of intensity values assigned to spatial coordinates, are imported into MATLAB as matrices of intensity information.

2) A threshold is then applied to this intensity information. The threshold limit in this case is 20% of the maximum chemiluminescence intensity for the given operating condition being evaluated. Consequently, intensities below this 20% threshold are set to zero and neglected. For instance, the combustor area downstream of shorter flames would not contribute to the flame's line of maximum intensity.

3) The radial coordinate of the maximum intensity for each axial location is determined, $r_m$. Plotting the $r_m$ values versus the axial coordinate system, x, results in the line of maximum intensity as seen in Figure **3-2a**.

4) Then, the formula to obtain the mean flame surface area, Equation **(3)**, is applied using the line of maximum intensity $r_m$ coordinates.

The mean flame surface area results for unforced flames obtained with the MATLAB program described above are shown in Figure **3-2b**. Flame surface area measurements, using arbitrary units, are compared for operating conditions with varying mean flow velocities and equivalence ratios. For a given equivalence ratio, the mean flame surface area increases linearly with mean flow velocity. At the same time, the mean flame surface area decreases with increasing equivalence ratio. This is consistent with the fact that the rate of heat release per unit flame surface area is greater for a flame with a higher equivalence ratio.

The second method to measure premixed flame heat release examines the turbulent flame area: the highly wrinkled portion of the flame located in the region of high chemiluminescence intensity surrounding the flame center of mass (COM). For this method, the remainder of the flame outside this high intensity region is neglected. Quantitatively, the cutoff point is chosen to be 70% of the maximum intensity of the operating condition. The region of high intensity, shown for example in Figure **3-3a**, is represented by the white and red area bounded by a superposed

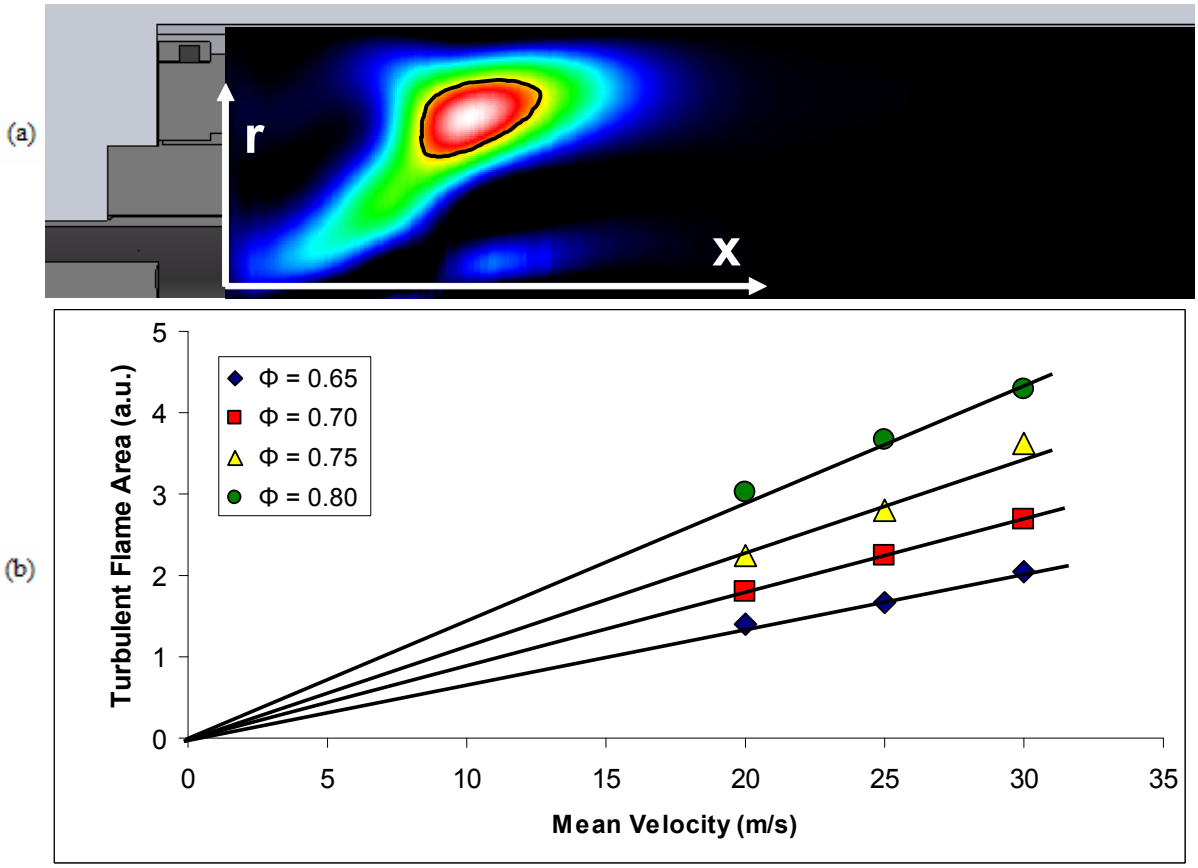


Figure **3-3**: (**a**) CH* deconvoluted chemiluminescence image illustrating the turbulent flame area measurement. Radial measurement *r* begins at the combustor centerline and extends to the edge of the quartz combustor. The variable *x* represents axial distance measured from the combustor dump plane. Operating conditions: $V_{mean}$ = 20 m/s and Φ = 0.75. (**b**) Turbulent flame area (arbitrary units) comparison for unforced flames with different mean equivalence ratios and velocities. Operating conditions: $V_{mean}$ = 20 m/s, 25 m/s, 30 m/s and Φ = 0.65, 0.70, 0.75, 0.80.

black boundary line. As mentioned previously, the intensity scales of the chemiluminescence images are presented in pseudo color, with white corresponding to the most intense regions of the flame and black representing the least intense. Looking at the chemiluminescence images shown in various figures, the high intensity region stretches from the white area to the inner edge of the orange region, colors representing intensities greater than 70% of the maximum intensity.

As with the flame surface area calculation, the radial component, r, is measured from the centerline of the combustor outward, and the axial component, x, is measured from the combustor

dump plane to the edge of the combustor. The formula to calculate the turbulent flame area ($A_{turb}$) is:

$$A_{turb} = \int_0^L \int_0^r 2\pi r I_{CH^*} dr dx \qquad (5)$$

where $I_{CH^*}$ is the intensity value for a given spatial coordinate (r,x). These values are weighted by the radial distance from the combustor centerline and summed over the high intensity region. Using a threshold technique, it is possible to sum only the values within the turbulent flame area. To obtain this result, a MATLAB program applies Equation **(4)** to the chemiluminescence image data. The details of this program can be broken down into a series of steps:

1) The chemiluminescence images, which are comprised of intensity values assigned to spatial coordinates, are imported into MATLAB as matrices of intensity information.

2) A threshold is then applied to this intensity information. The threshold limit in this case is 70% of the maximum chemiluminescence intensity for the given operating condition being evaluated. Consequently, intensities below this 70% threshold are set to zero and neglected, i.e., all data outside of the high intensity region.

3) Then, the formula to obtain the high intensity sum, Equation **(4)**, is applied using the intensity values, $I_{CH^*}$, at the spatial coordinates located within the high intensity region.

The turbulent flame area results for unforced flames obtained with the MATLAB program described above are shown in Figure **3-3b**. Turbulent flame area measurements, using arbitrary units, are compared for operating conditions with varying mean flow velocities and equivalence ratios. For a given equivalence ratio, the turbulent flame area within the COM region increases linearly with mean flow velocity. The rate at which the high intensity sum increases with mean velocity increases with increasing equivalence ratio, as indicated by the trend lines of Figure **3-3b** . The greatest equivalence ratio 0.80 of the figure corresponds to the trend line with the greatest slope.

In later sections, the procedures described above for calculating the mean flame area and the flame area associated with the turbulent wrinkling will be applied to flame forcing scenarios. The measurements will elucidate competing effects of two premixed flame response mechanisms, their constructive and destructive interactions influencing the gain of the flame transfer function.

### 3.2 Forcing Period Averaged ICCD Camera Chemiluminescence Imaging

In order to investigate the flame response mechanisms, global forcing period averaged chemiluminescence images are examined. The effect of velocity forcing frequency on average flame structure is investigated for the case of a normalized velocity fluctuation of 5% and a range of forcing frequencies from 0 Hz to 240 Hz. The results, which are presented in Figure **3-4**, show that the location of the flame's "center of mass" is very nearly constant over the range of operating conditions presented in the figure. In addition to the operating condition $V_{mean}$ = 30 m/s, $\Phi$ = 0.65 presented in the figure, this conclusion is true for all operating conditions examined at this forcing amplitude. So, given a 5% normalized velocity fluctuation, the flame length averaged over the forcing period will be constant regardless of frequency. The reason for choosing 5% for the forcing amplitude magnitude is because the magnitude is small enough to yield a flame response in the linear regime, and large enough to provide satisfactory signal coherence between the measured inlet velocity fluctuation and the measured overall chemiluminescence fluctuation. In the next section, flame transfer function measurements are presented with this same 5% velocity forcing amplitude. Therefore, the flame transfer function measurements presented in the next section will also have nearly constant flame length with respect to frequency. In a previous study conducted on a similar experimental facility, $L_{COM}$ was found to decrease with increasing forcing frequency [26]. The normalized velocity forcing amplitude in that case, however, was greater approximately 10%. When the experimental rig in

this study is forced at a comparable magnitude, the same result of decreasing $L_{COM}$ with increasing forcing frequency is found.

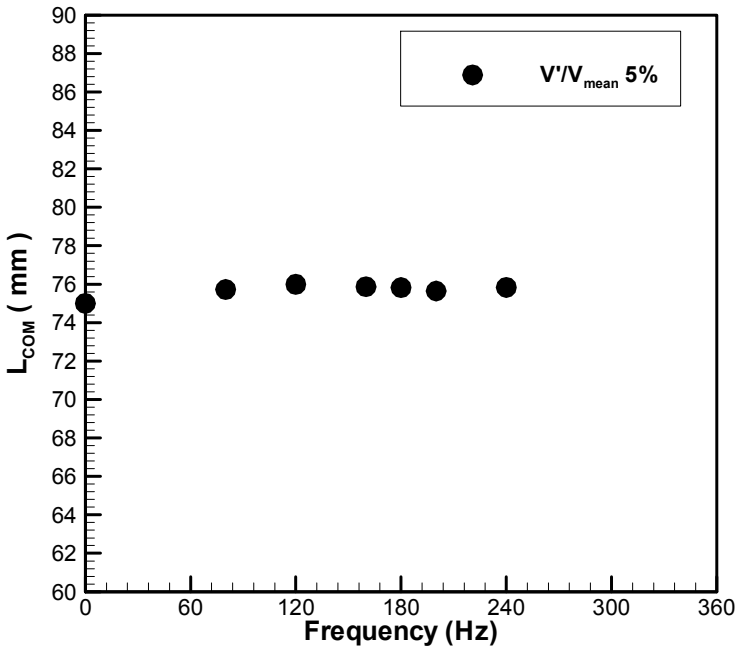


Figure **3-4**: Frequency dependence of flame length derived from forcing-period-averaged images. Operating condition: $V_{mean}$ = 30 m/s, $\Phi$ = 0.65.

### 3.3 Flame Transfer Function Fixed Velocity Forcing Amplitude

#### 3.3.1 Pressure Measurements

There were no observed self-excited instabilities at any of the operating conditions used in this study. Pressure measurements taken at the combustor did not show any significant, pressure fluctuations, i.e. $P'/P_{mean}$ >1%, for the operating conditions of interest. Checking for self-excited combustion instabilities was an important first step when taking flame transfer function (FTF) measurements, as these instabilities would skew the FTF measurement results.

Physically separated six inches from the exhaust section downstream, the combustor had an open end boundary condition. Therefore, the acoustics of the exhaust section did not affect the flame dynamics and FTF results.

### 3.3.2 Signal Coherence

A normalized inlet velocity forcing magnitude of $V'/V_{mean} = 5\%$ was chosen for the fixed forcing FTF measurements. Signal coherence at the fixed forcing amplitude between the chemiluminescence (output) and velocity (input) measurements would determine if the input signal amplitude was large enough to produce a meaningful output signal. A value of 1.0 would indicate that all of the power associated with the fluctuating velocity signal could be attributed to the effects of acoustic excitation [30]. Conversely, a value of 0.0 would suggest that the observed velocity fluctuations were merely due to flow turbulence. At most forcing frequencies, the coherence magnitudes were larger than 99%. At forcing frequencies which exhibited very small gain, the coherence did fall below 99%. This occurred because the chemiluminescence output data magnitudes themselves approached zero and background flow turbulence acted to distort the signal coherence because it had a similar order of magnitude. These forcing frequencies of very low magnitude gain will be discussed in the next section.

### 3.3.3 Flame Transfer Function Gain Versus Frequency

The flame transfer function (FTF) is obtained for a range of forcing frequencies with a fixed inlet velocity forcing amplitude of $V'/V_{mean} = 5\%$ at the forcing frequency. In general, the flame response exhibits behavior similar to an amplifier over a particular range of forcing frequencies, i.e. the flame's heat release fluctuation response is greater than the inlet velocity

fluctuation, and a low pass filter globally. The fact that the "V" flame can behave as an amplifier and a low pass filter was observed in laminar "V" flames in Schuller et al. [16]. Another feature of the FTF measurement, however, is also apparent. The gain versus frequency plot exhibits two peaks on either side of a frequency $f_{min}$, the frequency at which the gain reaches a minimum magnitude. Figure **3-5** compares the global CH* chemiluminescence FTF gain and phase for a fixed mean inlet velocity of 25 m/s at four different equivalence ratios. This figure also shows that as equivalence ratio increases, $f_{min}$ decreases and the magnitude of the second peak increases. As shown in the figure, $f_{min}$ was approximately 160 Hz for $\Phi = 0.80$, 180 Hz for $\Phi = 0.75$, 240 Hz for $\Phi = 0.70$, and 280 Hz for $\Phi = 0.65$. Since increasing the equivalence ratio decreases the overall flame length, as shown in Figure **3-1**, this suggests that flame structure, $L_{COM}$ in particular, affects the frequency $f_{min}$ as well as the magnitude of the higher frequency $2^{nd}$ peak. In addition, the maximum FTF gain increases with flame length, similar to Kim et al. [22].

Appendix **B,** Figures **B-1 – B-5**, presents data demonstrating the repeatability of the FTF results obtained from both CH* and OH* chemiluminescence measurements. For a given PMT calibration (see Section **2.3.3** for PMT calibration information), the FTF measurements are typically within ±4% of the averaged value. Since the CH* and OH* FTF results are similar, Figure **B-5**, only the CH* FTF results are presented.

In Section **3.1**, two overall flame shapes were described: a typical "V" flame and a "V" flame with a persistent extension into the outer corner recirculation zone. For the current FTF results, shorter flames with typical "V" flame shapes exhibit the $f_{min}$ bifurcation feature. For flames of the latter flame shape, the two peak behavior is diminished and the typical amplifier and low pass filter FTF behavior is observed. A physical description of this significantly damped gain response occurring at $f_{min}$ frequencies will be presented in a later section.

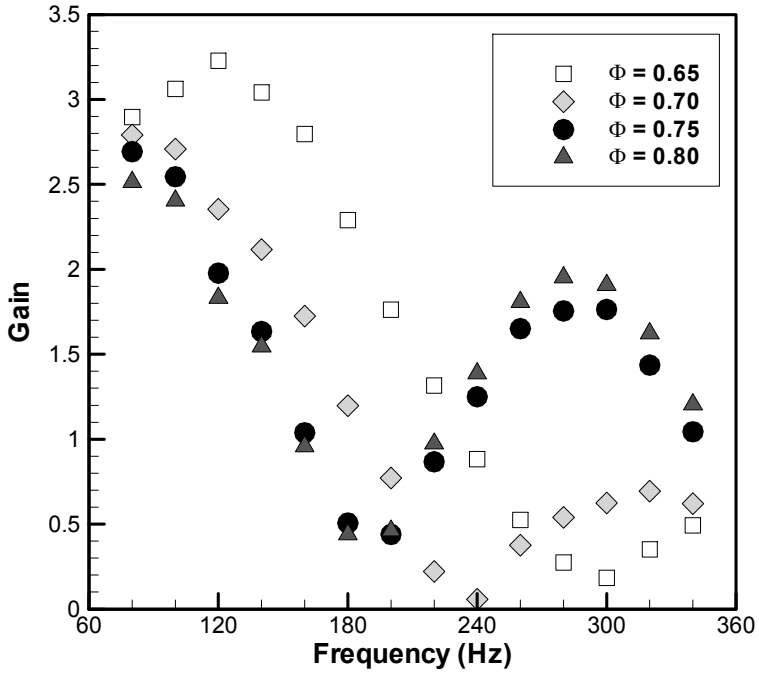


Figure **3-5**: Fixed forcing $V'/V_{mean}$ = 5% flame transfer function gain versus frequency. Operating conditions: $V_{mean}$ = 25 m/s, Φ = 0.65, 0.70, 0.75, and 0.80, frequency = 80 – 340 Hz.

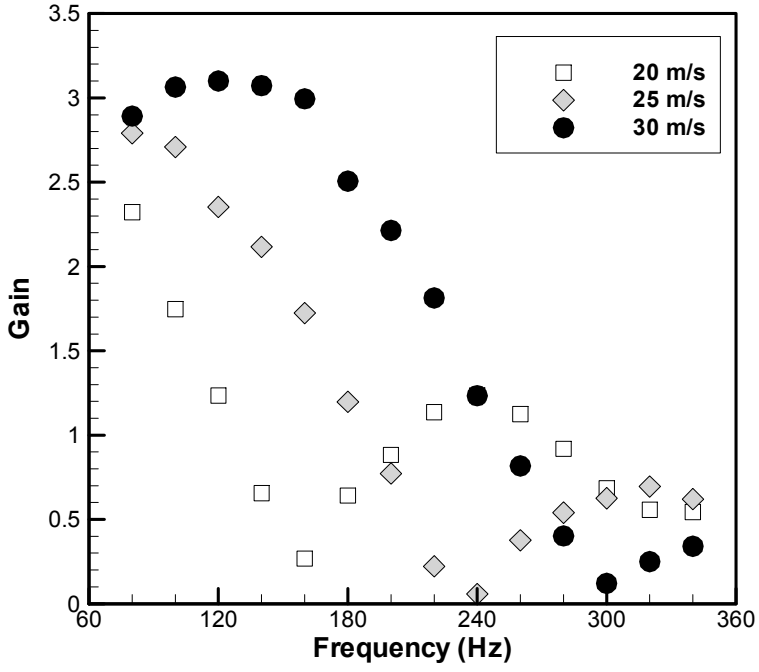


Figure **3-6**: Fixed forcing $V'/V_{mean}$ = 5% flame transfer function gain versus frequency. Operating conditions: Φ = 0.70, $V_{mean}$ = 20 m/s, 25 m/s, and 30 m/s, frequency = 80 Hz – 340 Hz.

In addition to flame length, mean flow velocity affects the frequency $f_{min}$. Figure **3-6** compares FTF gain for a mean equivalence ratio 0.70 and mean inlet velocities of 20 m/s, 25 m/s, and 30 m/s. Increasing the mean flow velocity has the effect of increasing the frequency $f_{min}$. This increase, however, is separate from the flame length's dependence on mean velocity, i.e., it was shown in Section **3.1** that increasing the mean flow velocity also increases the overall flame length. Figure **3-7** compares the length of the flame, $L_{COM}$, versus the frequency of near zero gain, $f_{min}$. The frequency $f_{min}$ took on multiple values for similar flame lengths. Therefore, flame length alone cannot be used to predict $f_{min}$. The mean flow velocity must also be considered, especially since this determines the convection speed of vorticity disturbances, to be explained in more detail in a later section. As stated in the Section **3.2**, the unforced flame $L_{COM}$ was comparable in magnitude to forced flame $L_{COM}$ for the velocity forcing amplitude of 5% (see Figure **3-4**). As a result, the unforced flame lengths are used when plotting Figure **3-7**. Another feature of the figure is that the frequency $f_{min}$ increases in an approximately linear fashion for a given mean velocity.

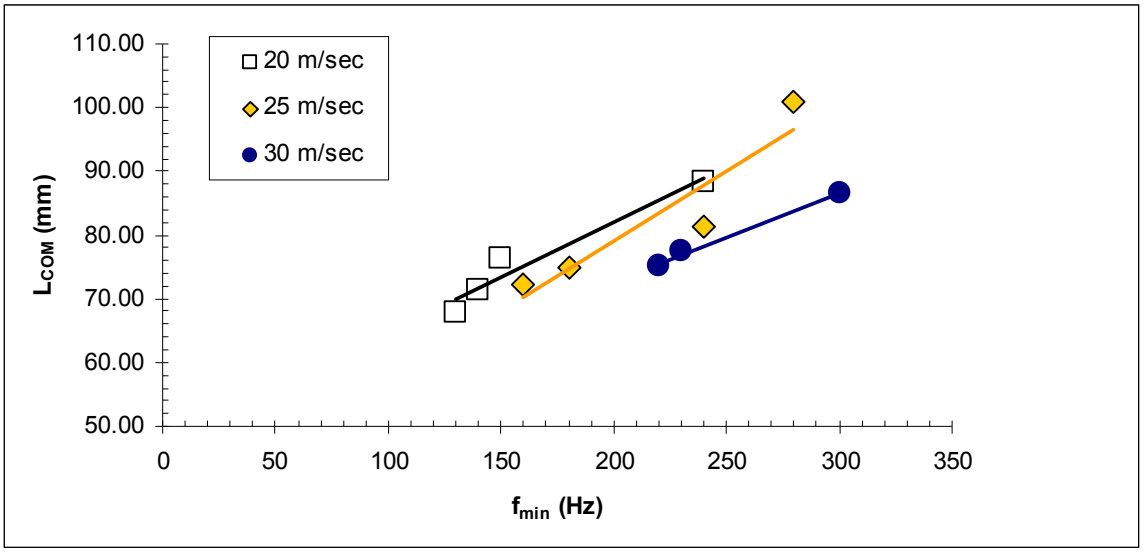


Figure **3-7**: Flame length versus $f_{min}$. Operating conditions: $V_{mean}$ = 20 m/s, 25 m/s, and 30 m/s, $\Phi$ = 0.65, 0.70, 0.75, and 0.80, $V'/V_{mean}$ = 5%.

Values for $f_{min}$ are presented for the operating conditions $V_{mean}$ = 20 m/s, 25 m/s, and 30 m/s and Φ = 0.65, 0.70, 0.75, and 0.80 in Table **3-2**. As observed in the previous figures, $f_{min}$ increases with flame length, but is also dependent on mean flow velocity. The operating condition $V_{mean}$ = 30 m/s and Φ = 0.65 does not have an $f_{min}$ frequency. This is because there is no second peak for this operating condition, and it would not be appropriate to define an $f_{min}$ because no minimum frequency is observed.

Figure **3-8** plots the gain and phase for the operating condition with no $f_{min}$ observed: $V_{mean}$ = 25 m/s and Φ = 0.65. As seen in the top part of the figure, at high frequencies, the gain tends towards zero and stays low. There is no second peak and there is also no phase discontinuity, a common feature for operating conditions with a frequency $f_{min}$. However, the phase, seen in the bottom of the figure, does tend to level off at higher frequencies, which also corresponds with a leveling off of the gain at higher forcing frequencies. FTF phase results will be further discussed in the next section.

Table **3-2**: Frequency, $f_{min}$. Operating conditions: $V_{mean}$ = 20 m/s, 25 m/s, 30 m/s and Φ = 0.65, 0.70, 0.75, 0.80.

| Φ / $V_{mean}$ | **0.65** | **0.70** | **0.75** | **0.80** |
|---|---|---|---|---|
| **20 m/sec** | 240 Hz | 150 Hz | 140 Hz | 130 Hz |
| **25 m/sec** | 280 Hz | 240 Hz | 180 Hz | 160 Hz |
| **30 m/sec** | - | 300 Hz | 230 Hz | 220 Hz |

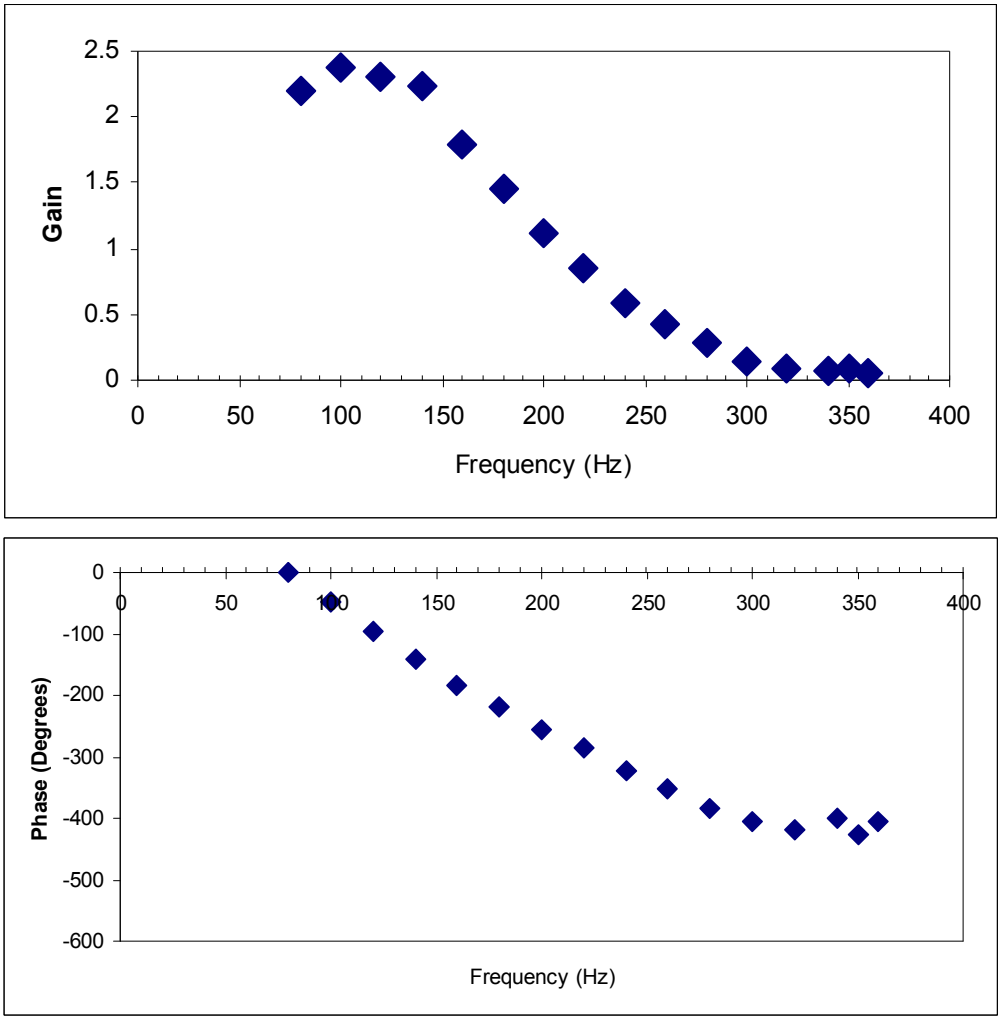


Figure **3-8**: Fixed forcing $V'/V_{mean}$ = 5% flame transfer function gain (top) and phase (bottom) versus frequency. Operating conditions: $V_{mean}$ = 30 m/s, $\Phi$ = 0.65, frequency = 80 – 360 Hz.

### 3.3.4 Flame Transfer Function Phase Versus Frequency

The FTF phase results corresponding to the constant mean inlet velocity FTF gain results discussed in the previous section are presented in Figure **3-9**. The FTF phase presented is the phase difference between the inlet velocity fluctuation and the chemiluminescence heat release

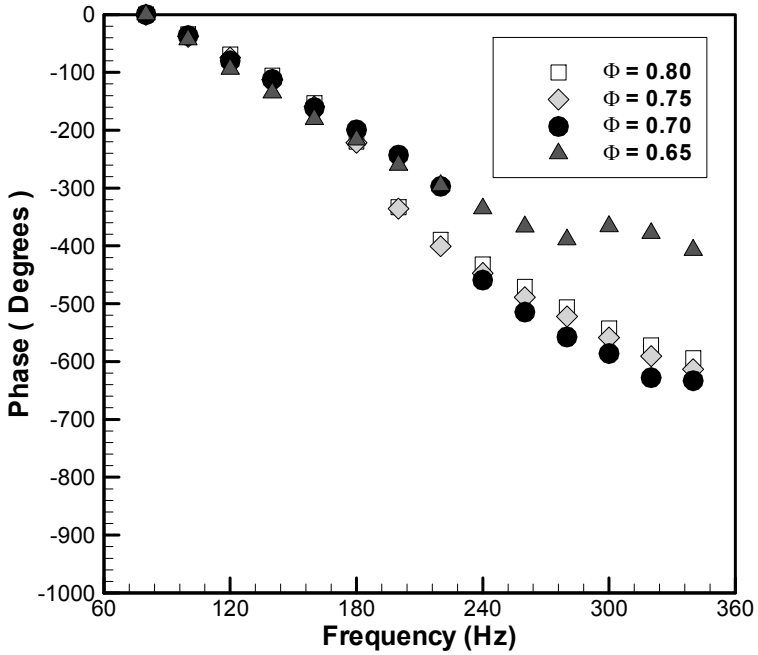


Figure **3-9**: Fixed forcing $V'/V_{mean}$ = 5% flame transfer function phase versus frequency. Operating conditions: $V_{mean}$ = 25 m/s, Φ = 0.65, 0.70, 0.75, and 0.80, frequency = 80 – 340 Hz.

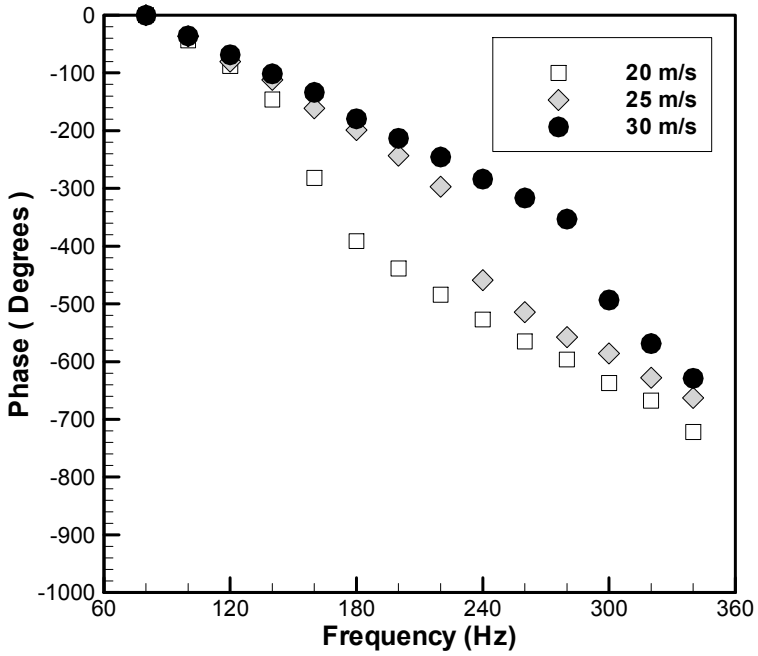


Figure **3-10**: Fixed forcing $V'/V_{mean}$ = 5% flame transfer function phase versus frequency. Operating conditions: Φ = 0.70, $V_{mean}$ = 20 m/s, 25 m/s, and 30 m/s, frequency = 80 Hz – 340 Hz.

response fluctuation. Except near $f_{min}$, the absolute phase increases linearly with forcing frequency, suggesting a constant convection time. Near $f_{min}$, the phase encounters a discontinuity of -180°, as predicted by Preetham et al. [14]. This discontinuity can be seen at f = 160 Hz, 180 Hz, 240 Hz, and 280 Hz for equivalence ratios of $\Phi$ = 0.80, 0.75, 0.70, and 0.65 respectively. Refer to Table **3-2** for a more comprehensive list of $f_{min}$ frequencies. In Figure **3-9**, the operating condition $V_{mean}$ = 25 m/s and $\Phi$ = 0.65 does not exhibit the 180° discontinuity at $f_{min}$ seen at operating conditions with higher equivalence ratios. Rather, the phase remains relatively constant with increasing frequency. As mentioned in Section **3.1**, the operating condition $V_{mean}$ =25 m/s and $\Phi$ = 0.65 exhibits a "V" flame with an extension into the outer corner recirculation zone. Figure **3-8**, of the previous section, provides another operating condition with the same flame shape and phase trend toward a constant value with increasing forcing frequency. This characteristic of the FTF phase at high frequencies for flames with this flame shape needs to be further investigated. In contrast, the shorter flame lengths with a typical "V" flame shape express 180° discontinuities at $f_{min}$, as seen in the higher equivalence ratio operating conditions in Figure **3-9,** starting at $\Phi$ = 0.70.

Similar FTF phase results are depicted in Figure **3-10** for different mean inlet velocities with a common equivalence ratio of $\Phi$ = 0.70. The absolute phase also increases linearly and encounters a -180° discontinuity at $f_{min}$. The flame shapes of the operating conditions presented in the figure are all of the typical shorter "V" flame shape.

### 3.3.5 Flame Transfer Function Generalization

In Sections **3.3.3** and **3.3.4** it was shown that the flame response is affected by the mean flow velocity in addition to flame length and overall flame shape. It was shown that the gain approached zero at a frequency that was defined as $f_{min}$. Twelve operating conditions were

investigated with a forced premixed flow velocity fluctuation amplitude normalized by the mean flow velocity, $V'/V_{mean}$, of 5%, mean flow velocities of 20 m/s, 25 m/s, and 30 m/s, and mean equivalence ratios of 0.65, 0.70, 0.75, and 0.80. The gains of those operating conditions versus frequency normalized by $f_{min}$ are superposed in Figure **3-11**, except the operating condition with a mean flow velocity of 30 m/s and an equivalence ratio of 0.65 is excluded because no $f_{min}$ was observed. As shown in the figure, the gain of all the flame transfer function results can be generalized in terms of $f_{min}$ when the frequency is less than or equal to $f_{min}$. The magnitude of the gain of the second peak occurring at frequencies greater than $f_{min}$ varies with operating condition. The peak is bounded with a maximum value of approximately 1.7 and a lower bound of approximately 0.3. So even though the gain increases with frequency greater than $f_{min}$, the gain decreases or levels off after the frequency of the second peak. Figure **3-12** shows that flame length and flame shape influence the trend in the gain of the second peak. The second peak maximum gain decreases with increasing flame length. Also, the high and low gain boundaries correspond to the two general flame lengths observed in Section **3.1**. The high boundary corresponds to the typical "V" flame shape and the low boundary corresponds to the longer length "V" flame shape with an extension into the corner recirculation zone.

### 3.4 Flame Response Mechanism Interaction

Premixed flame response to upstream inlet velocity fluctuations is primarily governed by two mechanisms: vorticity fluctuations and mean flame surface area fluctuations, acoustic disturbances affecting flame angle at the flame anchor point, as described in the Introduction. The former flame response mechanism arising from vorticity disturbances was presented in Durox et al. [10]. The latter, a flame perturbation originating at the root, was illustrated in Chaudhuri et al. [25] with line-of-sight CCD camera images, in Balachadran et al. [8] with OH

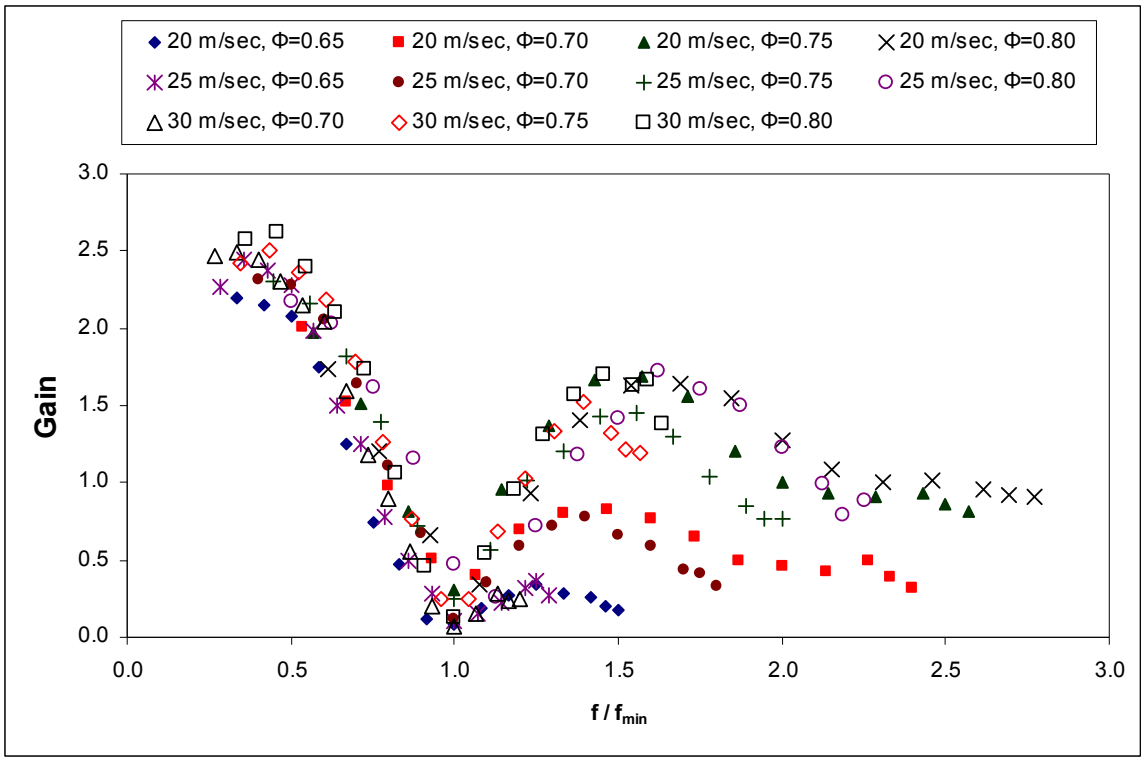


Figure **3-11**: Flame transfer function gain (CH*) versus normalized forcing frequency, $f/f_{min}$. Operating conditions: $V_{mean}$ = 20 m/s, 25 m/s, and 30 m/s, Φ = 0.65, 0.70, 0.75, and 0.80, $V'/V_{mean}$ = 5%.

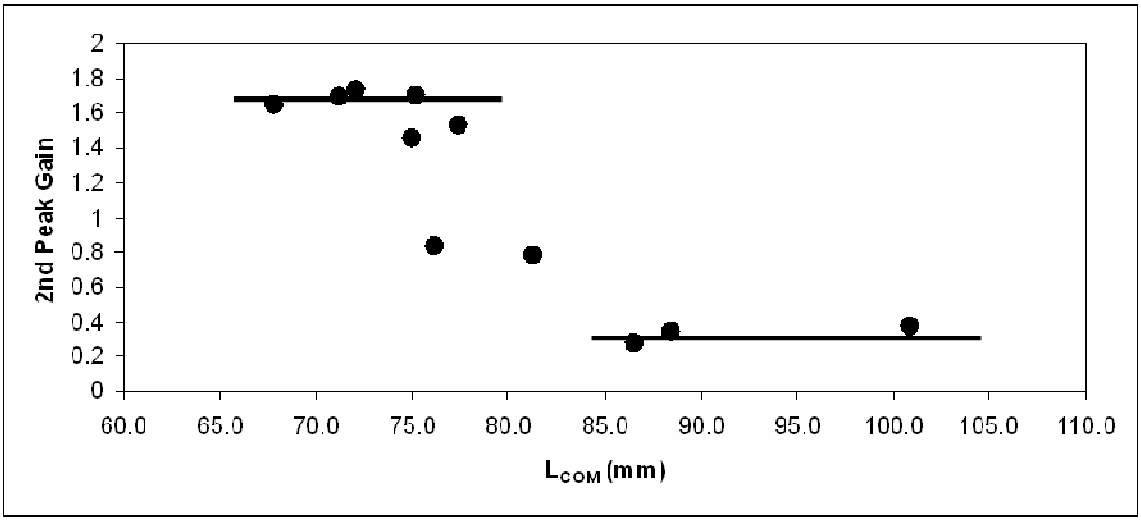


Figure **3-12**: Flame transfer function gain of 2nd peak versus flame length $L_{COM}$. Operating conditions: $V_{mean}$ = 20 m/s, 25 m/s, and 30 m/s, Φ = 0.65, 0.70, 0.75, and 0.80, $V'/V_{mean}$ = 5%.

PLIF images, and in Nottin et al. [31] with LES simulations. Preetham et al. [14] analytically described the constructive or deconstruction interaction of the two mechanisms. The study detailed two waves whose cancellation resulted in a significantly damped flame transfer function (FTF) gain. An experimental observation of such an interaction between the two flame response mechanisms will be presented in this section.

As mentioned previously, there were two general flame shapes observed: a typical "V" flame shape and a longer length "V" flame shape with an extension into the corner recirculation zone. The analysis of the flame response mechanisms, to be represented by the mean flame surface area and turbulent flame area measurements described earlier, will be presented for each of the two general observed flame shapes.

### 3.4.1 Typical "V" Flame Shape

In the previous section, the flame response was characterized in terms of a flame transfer function (FTF) exhibiting behavior as an amplifier for certain lower forcing frequencies and a low pass filter for higher forcing frequencies. The FTF also exhibited a significantly damped gain at a particular forcing frequency, $f_{min}$. Shorter flames, ones characterized by the typical "V" flame shape, had a second peak in gain at frequencies greater than $f_{min}$. One operating condition representative of this flame shape, mean inlet velocity 25 m/s and mean equivalence ratio 0.75 forced at a normalized velocity forcing amplitude of 5%, will be discussed in this section.

Figure **3-13** presents the FTF gain versus frequency plot for this example operating condition. Three scenarios, each representing a different regime of the flame transfer function, are identified: Scenarios A, B, and C. Scenario A, forcing frequency 100 Hz, represents the high gain regime at frequencies less than $f_{min}$. Scenario B, forcing frequency 180 Hz, represents the point of minimum gain at $f_{min}$. Scenario C, forcing frequency 260 Hz, represents the regime of

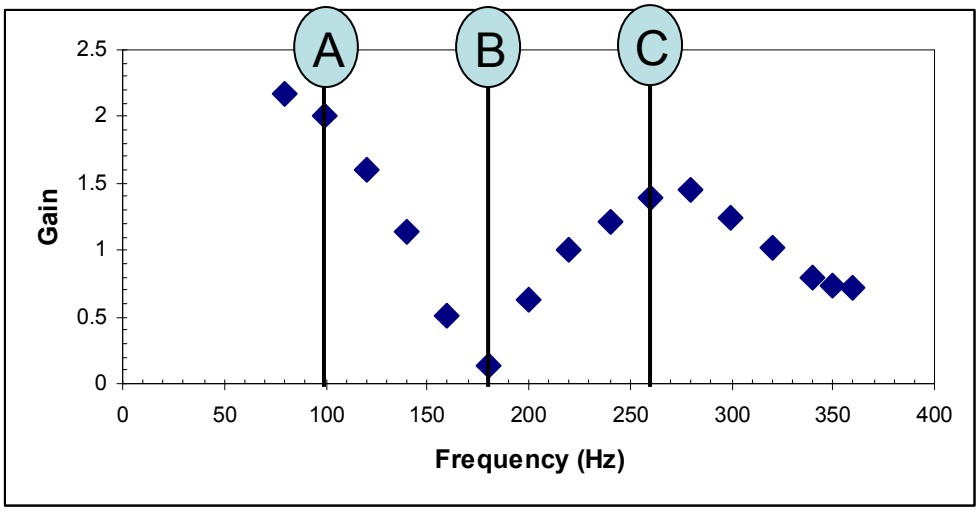


Figure **3-13**: Fixed forcing $V'/V_{mean}$ = 5% flame transfer function gain versus frequency. Scenario A = 100 Hz, Scenario B = 180 Hz, Scenario C = 260 Hz. Operating condition: $V_{mean}$ = 25 m/s, $\Phi$ = 0.75, frequency = 80 – 360 Hz.

the second peak in gain at frequencies greater than $f_{min}$. The methods to determine heat release described in Section **3.1**, mean flame surface area and turbulent flame area, will now be applied to each of the three aforementioned scenarios.

The methods for describing flame heat release, the mean flame surface area and turbulent flame area calculations, represent the two flame response mechanisms: mean flame surface area perturbations due to acoustic disturbances, and turbulent flame area perturbations due to vorticity disturbances [32]. The acoustic velocity disturbance mechanism is the effect of the velocity fluctuation on the mean flame area. Thus, the mean flame surface area measurement is used. The other flame response mechanism is the effect of vorticity fluctuations generated at the exit of the injector on local flame wrinkling. For a premixed flame, a highly wrinkled flame corresponds to greater heat release. Thus, the turbulent flame area, a measure of local flame wrinkling, is used.

To examine the flame response within a forcing period, CH* chemiluminescence images synchronized in phase with the inlet velocity fluctuation are employed. The flame images are averaged individual chemiluminescence images taken with a certain time delay after the velocity

fluctuation is registered. Since the fluctuation is periodic, the camera will catch the flame at the same instant in its periodic motion for every image. In this case, phase synchronized images were taken at 30° intervals. For Scenario A, phase synchronized images are presented in Figure **3-14**. The high intensity region, shown in white and red, along with the entire flame brush itself, fluctuate throughout the forcing period.

From the chemiluminescence intensity data obtained from these images, quantitative measurements can be derived such as the mean flame surface area (Mean SA), total CH* intensity, flame center of mass (COM), and the turbulent flame area (Turb Area) fluctuation measurements. For Scenario A, these fluctuations normalized by their mean values are presented versus phase in Figure **3-15**. In this case, all four quantitative measures fluctuate in a similar manner within the forcing period, as indicated by their magnitude versus phase relationships. The total normalized chemiluminescence intensity fluctuates between 1.10 and 0.90, which is to be expected because the gain at this frequency is 2, twice the input velocity amplitude of 0.05. The fluctuation in the flame COM, flame length, indicates that the entire flame brush is moving throughout the forcing period. Representing the two flame response mechanisms, the mean flame surface area and turbulent flame area measurements interact constructively. In Scenario A, changes in total CH* intensity are correlated with the two flame response mechanisms. When the normalized fluctuation magnitudes of the mechanisms are at a maximum, the total intensity measurement magnitude is at a maximum and vice versa. The magnitudes of the two flame mechanisms are correlated, but are not directly additive, however, to the magnitude of the total CH* intensity measurements. The normalized turbulent flame area fluctuation has a greater amplitude, approximately 20%, compared to the mean flame surface area amplitude, approximately 10%.

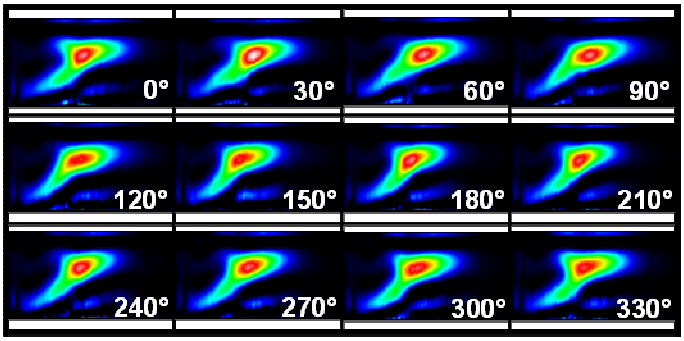


Figure **3-14**: Scenario A - 100 Hz forcing frequency. Deconvoluted CH* images phase-synchronized with the velocity fluctuation. Operating condition: 25 m/s, Φ = 0.75, frequency = 100 Hz, $V'/V_{mean}$ = 5%.

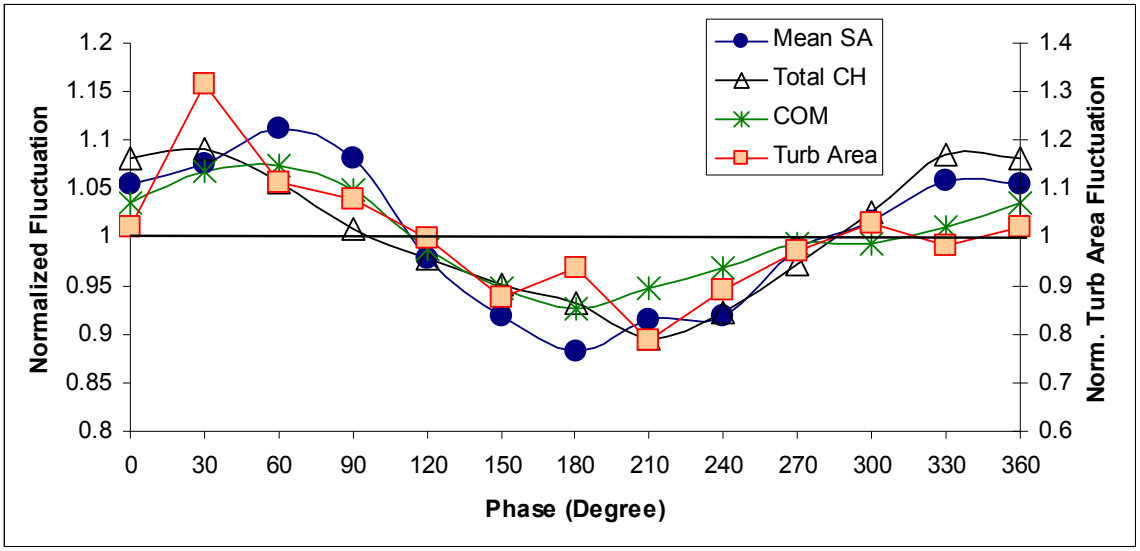


Figure **3-15**: Scenario A - 100 Hz forcing frequency. Normalized mean flame surface area (Mean SA), total CH* image intensity, flame length center of mass (COM), and turbulent flame area (Turb Area) fluctuations versus phase. Operating condition: 25 m/s, Φ = 0.75, frequency = 100 Hz, $V'/V_{mean}$ = 5%.

It should be noted that there are two different vertical axes in Figure **3-15**. The vertical axis on the right side is exclusively utilized for the turbulent flame area measurement, while the vertical axis on the left is utilized for the other normalized fluctuations. This secondary vertical axis on the right side is required because the magnitudes of the normalized turbulent flame area fluctuations are greater than those of the other normalized fluctuations. Therefore, all of the following normalized fluctuation plots will feature the two separate vertical axes for enhanced comparison clarity.

Scenario B represents the minimum gain flame response at the forcing frequency $f_{min}$, 180 Hz for this operating condition. Phase synchronized images are presented in Figure **3-16**. The normalized fluctuation plot is shown in Figure **3-17**. In this case, the total CH* intensity varies little throughout the forcing period, supporting the fact that the flame transfer function gain is minimal at this forcing frequency. In contrast to Scenario A, Scenario B features mean flame surface area and turbulent flame area measurements with dissimilar phase characteristics. The maximum of the mean flame surface area fluctuation occurs when the turbulent flame area fluctuation is at a minimum. The mean flame surface area fluctuation is the result of acoustic velocity fluctuations which cause the flame angle at the base of the flame to fluctuate. The flame angle fluctuations travel convectively along the flame front, producing a fluctuation in the mean flame area. The acoustic velocity fluctuations also result in periodic vorticity generation in the shear layer near the exit of the injector. The regions of high and low vorticity are convected to the flame front where they produce variations in the turbulent flame area. The vorticity perturbation originates at the corner of the dump plane, while the flame angle fluctuation originates at the corner of the centerbody. When the mean flame area and the turbulent flame area fluctuations occur at the same time (in-phase) the gain is at a maximum. While when the fluctuations are 180 degrees out of phase the gain is at a minimum. It is also important to note the similar magnitudes of the heat release response

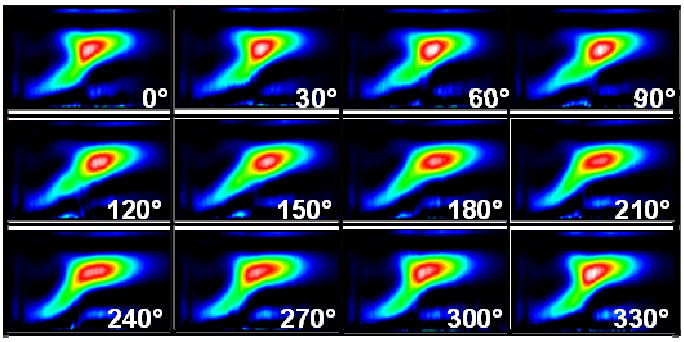


Figure **3-16**: Scenario B - 180 Hz forcing frequency. Deconvoluted CH* images phase-synchronized with the velocity fluctuation. Operating condition: 25 m/s, Φ = 0.75, frequency = 180 Hz, $V'/V_{mean}$ = 5%.

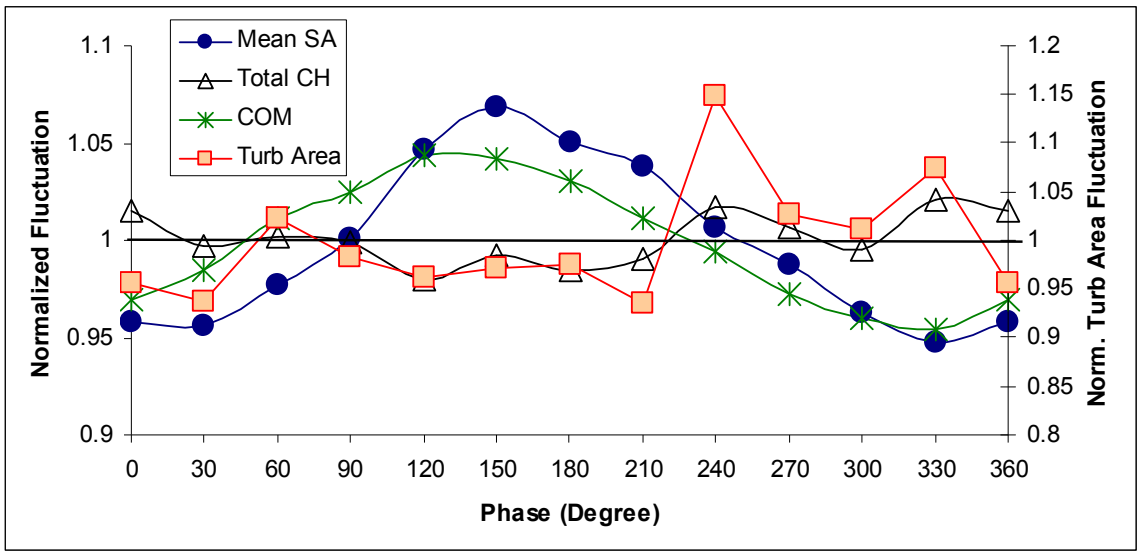


Figure **3-17**: Scenario B - 180 Hz forcing frequency. Normalized mean flame surface area (Mean SA), total CH* image intensity, flame length center of mass (COM), and turbulent flame area (Turb Area) fluctuations versus phase. Operating condition: 25 m/s, Φ = 0.75, frequency = 180 Hz, $V'/V_{mean}$ = 5%.

measurements. The normalized flame surface area and turbulent flame area fluctuations have similar magnitudes in Scenario B. So, the two flame response mechanisms interact destructively without one mechanism overpowering the other.

Scenario C represents the second peak regime of the flame transfer function versus gain, i.e., the frequency, 260 Hz, is greater than $f_{min}$. Phase synchronized images are presented in Figure **3-18**. The normalized fluctuation plot is shown in Figure **3-19**. In this case, the total CH* chemiluminescence intensity amplitude is greater than 0.05, but is not as large as that of Scenario A. The two flame response mechanisms, mean flame surface area and turbulent flame area fluctuations, interact constructively. The turbulent flame area measurement has a similar magnitude to that of Scenario A, while the mean flame surface area fluctuation magnitude is approximately 50% of that of Scenario A. Also in Figure **3-19**, the COM does not fluctuate throughout the forcing period. At this higher forcing frequency, the entire flame brush has less time to react and move throughout the forcing period.

For flames having the typical "V" flame shape, it was shown that when the two flame response mechanisms, mean flame surface area fluctuations and turbulent flame area fluctuations interact constructively; the overall flame heat release response is amplified, as seen in Scenarios A and C, Figure **3-13**. When the two flame response mechanisms interact destructively, the overall flame heat release response is reduced, as seen in Scenario B in Figure **3-13**. Flame response mechanism interaction for flames having the second general flame shape, as mentioned in Section **3.1**, will be discussed in the next section.

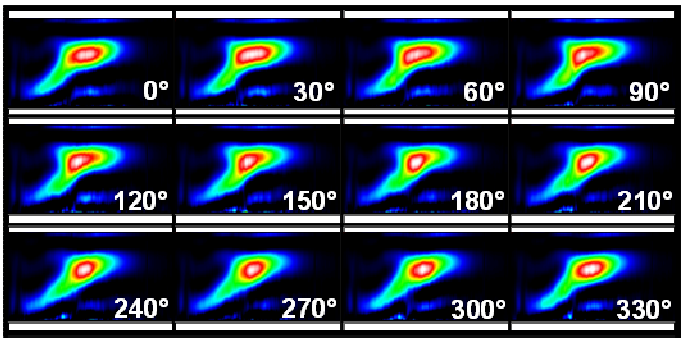


Figure **3-18**: Scenario C - 260 Hz forcing frequency. Deconvoluted CH* images phase-synchronized with the velocity fluctuation. Operating condition: 25 m/s, Φ = 0.75, frequency = 260 Hz, $V'/V_{mean}$ = 5%.

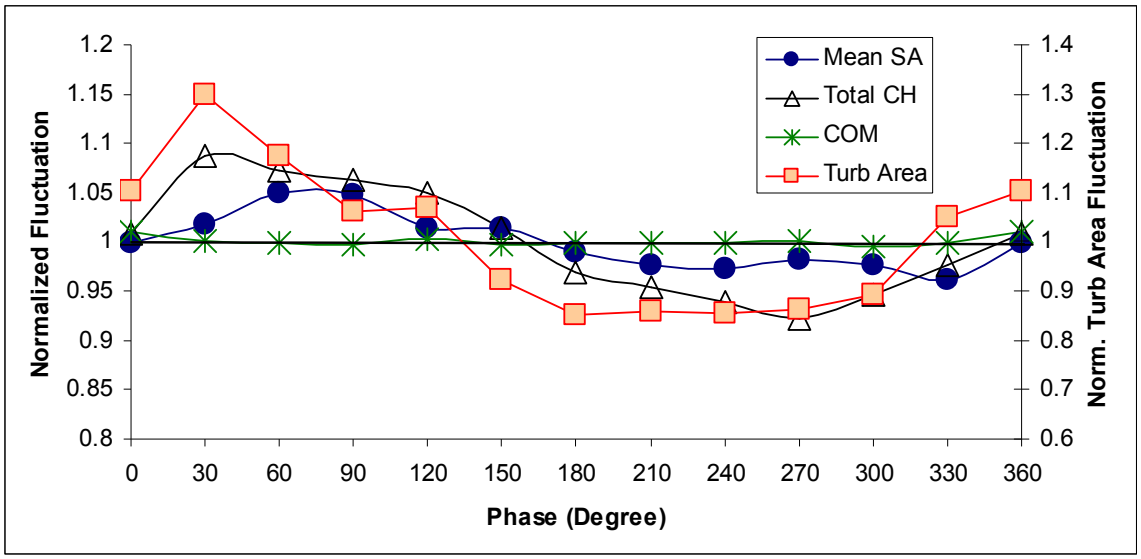


Figure **3-19**: Scenario C - 260 Hz forcing frequency. Normalized mean flame surface area (Mean SA), total CH* image intensity, flame length center of mass (COM), and turbulent flame area (Turb Area) fluctuations versus phase. Operating condition: 25 m/s, Φ = 0.75, frequency = 260 Hz, $V'/V_{mean}$ = 5%.

### 3.4.2 Longer "V" Flame Shape with Extension into Corner Recirculation Zone

The interaction of the two premixed flame response mechanisms, mean flame surface area and turbulent flame area fluctuations, for the longer "V" flame shape with an extension into the corner recirculation zone is presented in this section. The operating condition representative of this flame shape is: mean inlet velocity 25 m/s and mean equivalence ratio 0.65 forced at a normalized velocity forcing amplitude of 5%.

Figure **3-20** presents the FTF gain versus frequency plot for this long length flame shape operating condition. Two scenarios, each representing a different regime of the flame transfer function, are identified: Scenarios D and E. Scenario D, forcing frequency 180 Hz, represents the high gain regime at frequencies less than $f_{min}$. Scenario E, forcing frequency 280 Hz, represents the point of minimum gain at $f_{min}$. For this operating condition, no second peak is observed. The same methodology for phase synchronized image analysis and quantitative data extraction from Section **3.4.1** will now be applied to each of the two aforementioned scenarios.

Scenario D represents the high gain regime for frequencies less than $f_{min}$, in this case 180 Hz. The overall flame shape is different compared to the previous section as seen in the phase synchronized images presented in Figure **3-21**. Significant changes in the high intensity region of the flame are observed. A large red and white area can be seen in the image at 240° while the high intensity region nearly vanishes in the image at 90°. This behavior can also be seen quantitatively with the turbulent flame area fluctuations in the normalized fluctuation plot shown in Figure **3-22**.

For this scenario, the total CH* chemiluminescence intensity amplitude is slightly larger than 0.10, more than twice the input velocity amplitude of 0.05. Thus, the gain of the flame transfer function is between 2 and 2.5. The flame center of mass (COM) fluctuates throughout

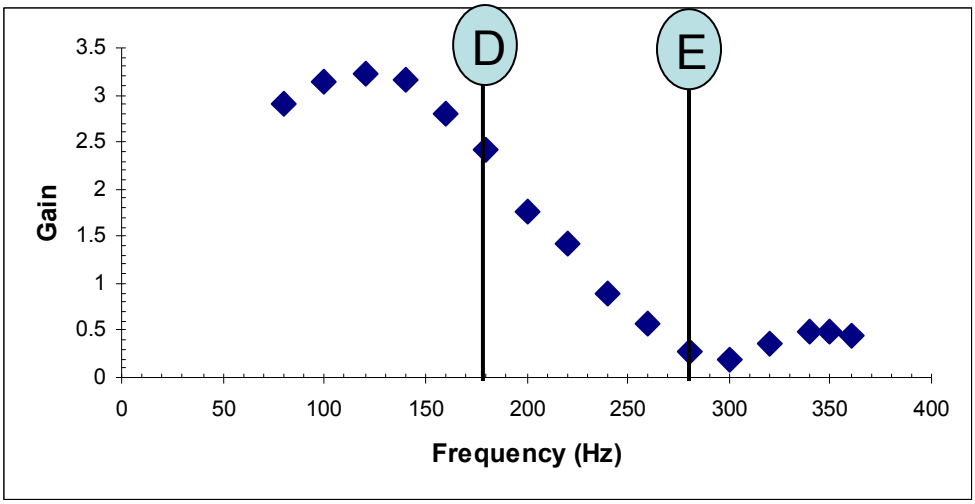


Figure **3-20**: Fixed forcing V'/$V_{mean}$ = 5% flame transfer function gain versus frequency. Scenario D = 180 Hz, Scenario E = 280 Hz. Operating condition: $V_{mean}$ = 25 m/s, Φ = 0.65, frequency = 80 – 360 Hz.

the forcing period. Interestingly, the two flame response mechanisms, interact destructively in this case. If everything else were identical as Scenario B, then the gain should be minimal. However, in Scenario D, the magnitude of the normalized turbulent flame area fluctuation is far greater than the magnitude of the normalized mean flame surface area fluctuation. The vertical axis on the right corresponds to the turbulent flame area while the vertical axis on the left corresponds to the other three normalized fluctuations. So, the flame turbulent area measurement has an amplitude of 0.80, while the flame surface area measurement has an amplitude of 0.05, a very significant difference. Despite the fact that the two flame mechanisms interacted destructively, the difference in the relative magnitudes of the two normalized fluctuation magnitudes results in an amplified net heat release response. Since the large magnitude of the HIS flame response fluctuation is responsible for the net flame heat release response, the total CH* intensity fluctuation correlates with the flame turbulent area fluctuation in Figure **3-22**. The total intensity fluctuation is greatest when the magnitude flame turbulent area fluctuation is greatest and vice versa.

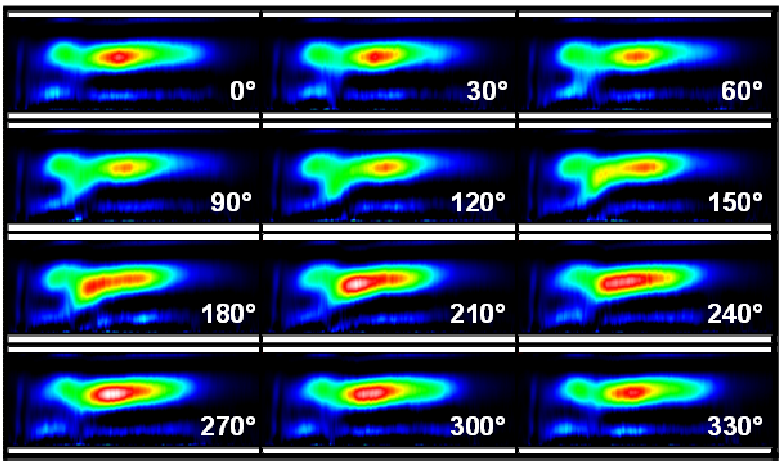


Figure **3-21**: Scenario D - 180 Hz forcing frequency. Deconvoluted CH* images phase-synchronized with the velocity fluctuation. Operating condition: 25 m/s, Φ = 0.65, frequency = 180 Hz, $V'/V_{mean}$ = 5%.

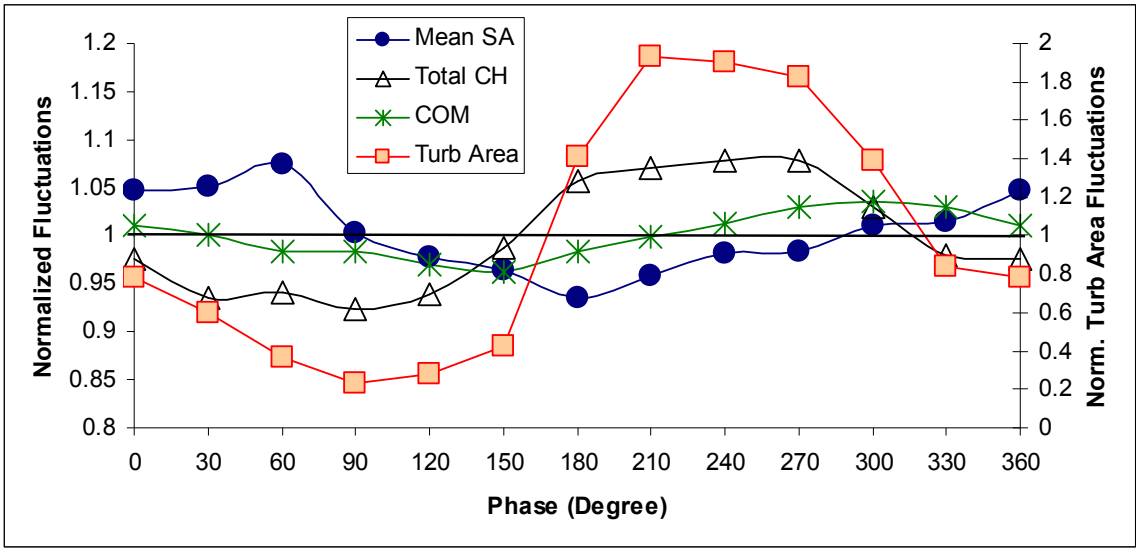


Figure **3-22**: Scenario D - 180 Hz forcing frequency. Normalized mean flame surface area (Mean SA), total CH* image intensity, flame length center of mass (COM), and turbulent flame area (Turb Area) fluctuations versus phase. Operating condition: 25 m/s, Φ = 0.65, frequency = 180 Hz, $V'/V_{mean}$ = 5%.

Scenario E represents the minimum gain flame response at the forcing frequency $f_{min}$, 280 Hz for this operating condition. Phase synchronized images are presented in Figure **3-23**. Changes in the high intensity region of the flame images are less pronounced than those in Figure **3-21**. The region is more consistent throughout the forcing period. This behavior can also be seen quantitatively with the turbulent flame area fluctuations in the normalized fluctuation plot shown in Figure **3-24**.

In Scenario E, the total CH* chemiluminescence intensity amplitude and the flame transfer function gain is minimal. Similar to Scenario C, the flame center of mass (COM) does not fluctuate throughout the period. In general, for the operating conditions observed, the flame COM ceases to fluctuate within the forcing period at higher frequencies. The two flame response mechanisms interact destructively in this case, similar to Scenario D. In Scenario E, however, the difference in the relative magnitudes of the fluctuations is far less pronounced. The scale of the right axis in Figure **3-24** is the same as that of Figure **3-22** to emphasize the difference in the turbulent flame area fluctuation magnitudes. Since the relative magnitudes of the two flame response mechanisms are comparable, the destructive interaction results in a minimal gain, similar to Scenario B.

Scenarios D and E show that flame shape needs to be considered when examining premixed flame response mechanisms. For longer "V" flame shapes with an extension into the corner recirculation zone, vorticity fluctuations, indicated by the turbulent flame area measurement, are amplified far greater than mean flame surface area fluctuations. This could be due to the fact that the long flame's mean flame location is constrained by the combustor wall In addition, despite the fact that the two flame response mechanisms may interact destructively, the high relative magnitude of one flame response mechanism may overpower the other to yield a net flame heat release response.

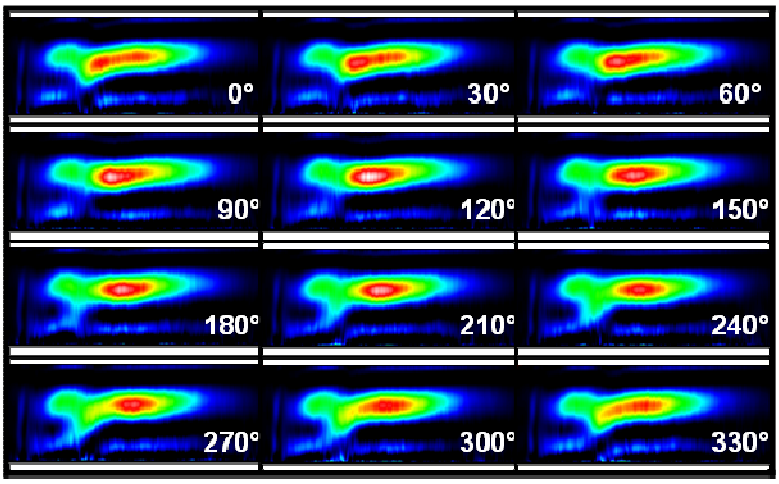


Figure **3-23**: Scenario E - 280 Hz forcing frequency. Deconvoluted CH* images phase-synchronized with the velocity fluctuation. Operating condition: 25 m/s, Φ = 0.65, frequency = 280 Hz, $V'/V_{mean}$ = 5%.

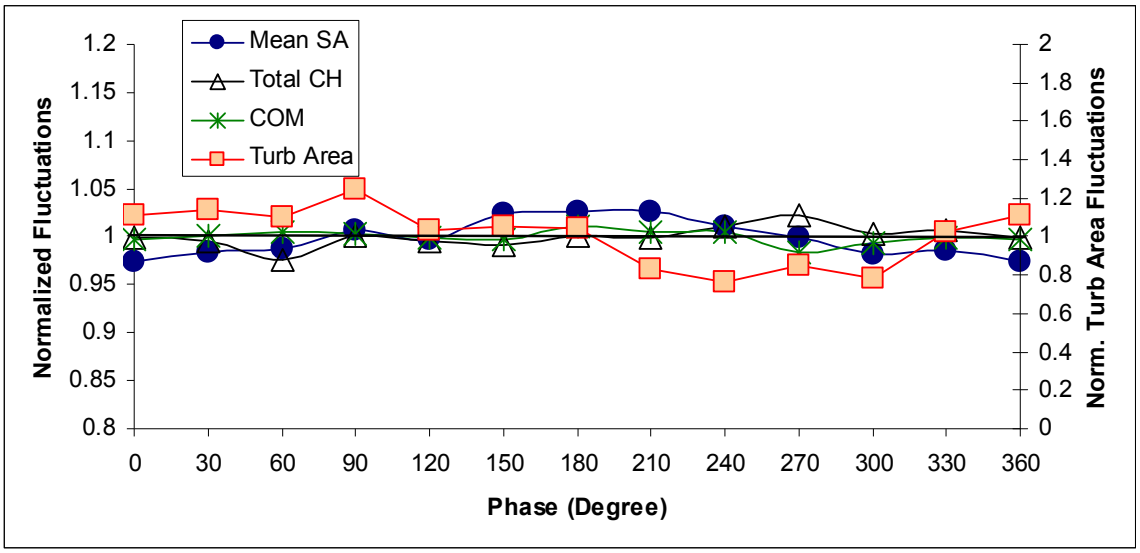


Figure **3-24**: Scenario E - 280 Hz forcing frequency. Normalized mean flame surface area (Mean SA), total CH* image intensity, flame length center of mass (COM), and turbulent flame area (Turb Area) fluctuations versus phase. Operating condition: 25 m/s, Φ = 0.65, frequency = 280 Hz, $V'/V_{mean}$ = 5%.

### 3.5 Effect of Forcing Amplitude on Flame Response Mechanism Interaction

The previous section dealt with operating conditions with a fixed velocity forcing amplitude, $V'/V_{mean} = 5\%$. This section will investigate the effect of altering the velocity forcing amplitude while keeping the other operating conditions constant. A typical "V" flame shape will be examined. In fact, the same forcing frequencies that were examined in Figure **3-13** from Section **3.4.1** will be examined in this section.

Figure **3-25** compares the normalized chemiluminescence intensity response due to inlet velocity fluctuations for three different forcing frequencies: 100 Hz, 180 Hz, and 260 Hz. The three frequencies chosen are less than, equal to, and greater than the forcing frequency at the minimum gain, $f_{min}$, respectively. The maximum inlet velocity forcing amplitude is limited by the hardware rather than flame blowoff. As shown in Figure **3-25**, the normalized chemiluminescence intensity response at 100 Hz increases linearly over the entire range of forcing amplitudes tested. At the 260 Hz forcing frequency, the chemiluminescence intensity response increases linearly with frequency until exhibiting the onset of non-linear behavior at a forcing amplitude of approximately 16%, similar to Bellows et al. [9]. The higher forcing frequency 260 Hz data reaches a nonlinear regime at a lesser velocity forcing amplitude than the lower forcing frequency conditions: 180 Hz reaches it at 20% and 100 Hz does not attain a nonlinear response for forcing amplitudes less than 44%. The chemiluminescence intensity response at 180 Hz requires additional explanation and will be discussed in the next paragraph.

Three regimes of heat release response, Regimes I – III, dependent on velocity forcing amplitude, can be observed for the forcing frequency $f_{min}$, approximately 180 Hz. As shown in Figure **3-25**, the chemiluminescence intensity response, heat release rate response, is minimal in Regime I. Section **3.4.1** attributed the destructive interactions of two flame response mechanisms as the cause for the minimal gain for this regime.

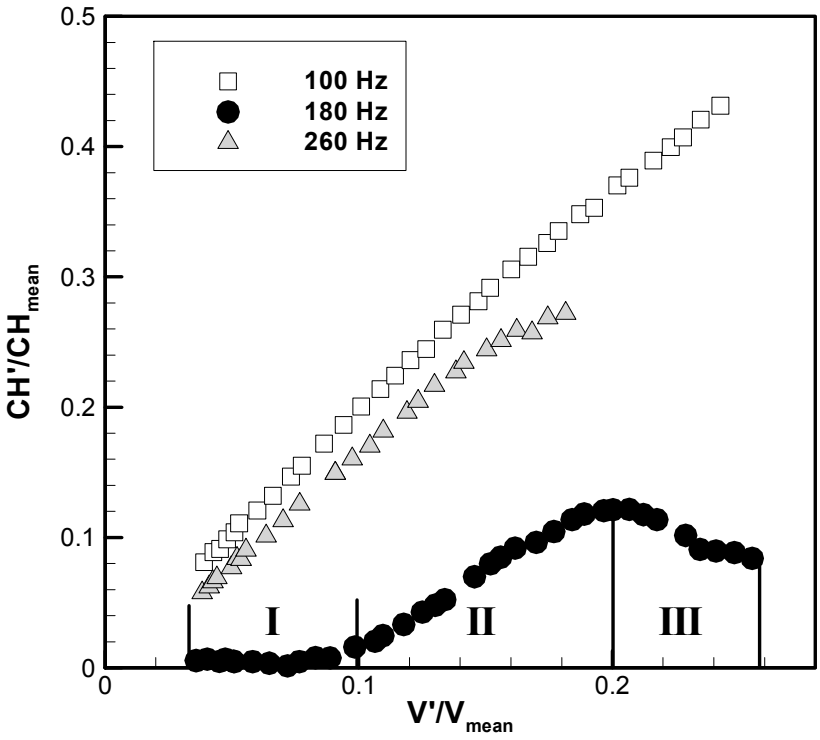


Figure **3-25**: Normalized chemiluminescence response due to varying magnitude of inlet velocity fluctuations. Operating conditions: 25 m/s, Φ = 0.75, forcing frequencies = 100 Hz, 180Hz, 260 Hz, and $V'/V_{mean}$ = Regime I (0.04 – 0.10), Regime II (0.10 – 0.20), Regime III (0.20 – 0.26).

In the next regime, Regime II, the heat release fluctuation increases almost linearly with increasing velocity forcing amplitude. The flame response remains damped, however, when compared to other forcing frequencies. To further investigate the flame response mechanisms' interaction, phase synchronized images are presented in Figure **3-26**. The overall shape of the flame brush changes more drastically throughout its forcing period when compared to phase synchronized images from Regime I presented in Figure **3-16** from Section **3.4.1**, where the overall shape of the flame brush appears more consistent.

From the chemiluminescence intensity data obtained from these images, fluctuations normalized by their mean values of the following quantitative measurements are plotted versus phase in Figure **3-27**: mean flame surface area (Mean SA), total CH* intensity, flame center of

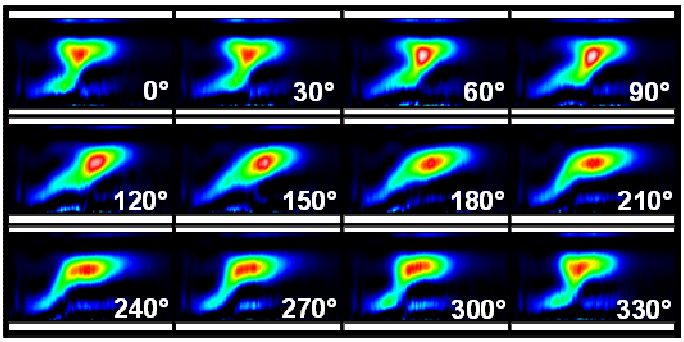


Figure **3-26**: Regime II - Deconvoluted CH* images phase-synchronized with the velocity fluctuation. Operating condition: 25 m/s, Φ = 0.75, frequency = 280 Hz, $V'/V_{mean}$ = 13%.

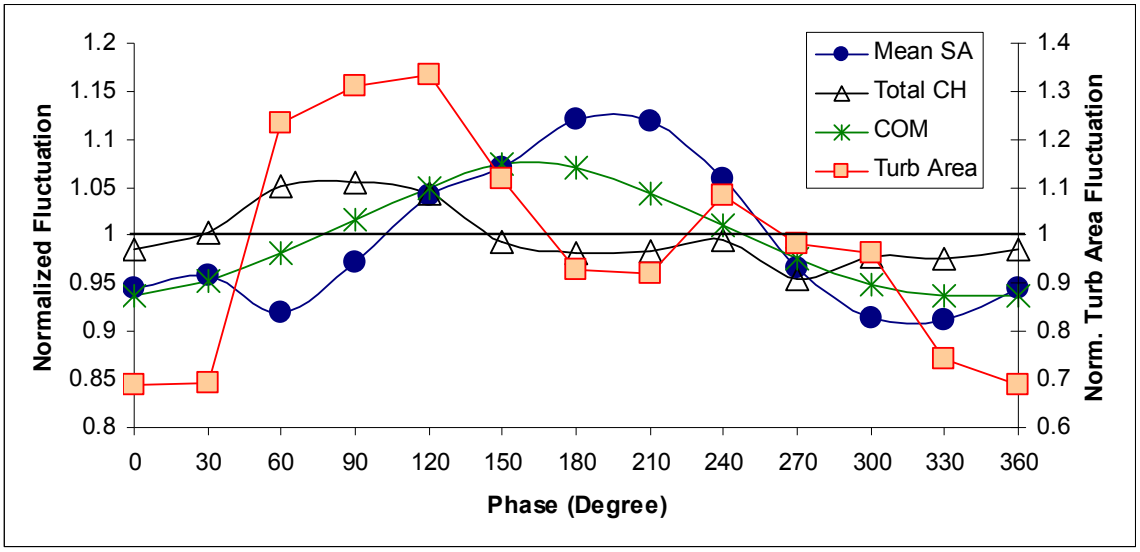


Figure **3-27**: Regime II - Normalized mean flame surface area (Mean SA), total CH* image intensity, flame length center of mass (COM), and turbulent flame area (Turb Area) fluctuations versus phase. Operating condition: 25 m/s, Φ = 0.75, frequency = 180 Hz, $V'/V_{mean}$ = 13%.

mass (COM), and the turbulent flame area (Turb Area). The vertical scale on the right is exclusive to turbulent flame area fluctuations while the vertical scale on the left applies to the other fluctuations in the figure. The total CH* chemiluminescence intensity amplitude is approximately 0.05, which is still less than input velocity amplitude of 0.13. The flame COM fluctuates throughout the period. The two flame response mechanisms, mean flame surface area perturbations originating at the flame root and vorticity perturbations, which are indicated as the turbulent flame area, do not interact constructively. At the same time, the phase relationship is not entirely destructive. The two flame response mechanism indicators have similar magnitudes. So, the partially constructive interaction of two flame response mechanisms yields a net flame heat release response, but the response is reduced compared to the input velocity fluctuation magnitude.

Preetham et al. [14] suggests that the $f_{min}$ frequency shifts to a higher frequency when the velocity amplitude is increased. This is due to the different relative "ages" of the flame response mechanisms. Although both flame response mechanisms travel at flow convection velocity, these originate at different locations. The flame angle mean flame surface area fluctuation originates at the corner of the centerbody, while the vorticity fluctuation originates a the corner of the dump plane. Further explanation of Preetham et al.'s findings, along with a figure demonstrating the $f_{min}$ shift concept, Figure **1-8**, can be found in Section **1.3**. So, the change in chemiluminescence intensity response between Regime I and Regime II in Figure **3-25** may be due to the fact that the $f_{min}$ has shifted to a higher frequency. Further investigation of this possible shift in $f_{min}$ is beyond the scope of this work.

Finally, at the highest observed forcing velocity amplitudes, Regime III, the heat release response saturates and even decreases with increasing velocity forcing. Nonlinear response has been observed to involve a decreased heat release response at high forcing amplitudes following

the saturation regime [33]. Frequently, vortex shedding occurs in operating conditions with large forcing amplitudes and causes flame response nonlinearity [8]. Figure **3-28** reveals that vortex shedding is indeed the observable cause for the nonlinear response of Regime III. Phase synchronized chemiluminescence images expose discrete high intensity regions, which are representative of coherent large-scale vortex structures, separating from the dump plane and joining the discrete high intensity region shed in the previous forcing period.

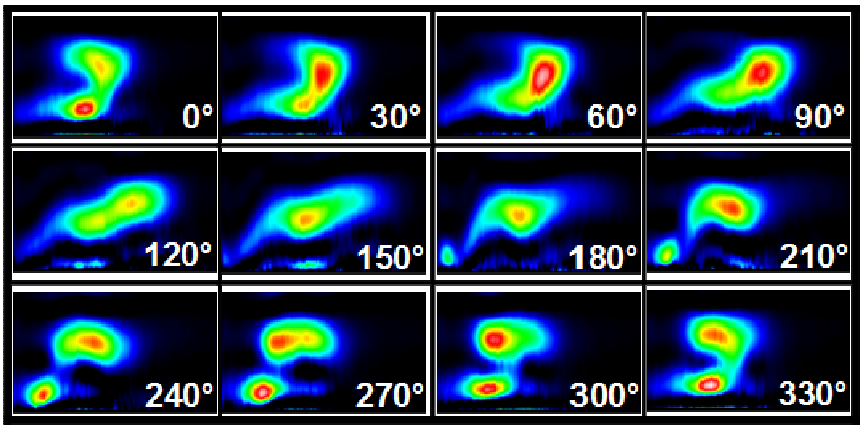


Figure **3-28**: Regime III - Deconvoluted CH* images phase-synchronized with the velocity fluctuation. Operating condition: 25 m/s, $\Phi = 0.75$, frequency = 180 Hz, $V'/V_{mean} = 25\%$.

# Chapter 4

# Conclusions and Suggestions for Future Studies

## 4.1 Conclusions

An experimental study was conducted of the interaction between two premixed forced flame response mechanisms: mean flame surface area perturbations due to velocity fluctuations, and turbulent flame area fluctuations which are the result of periodic vorticity generation in the shear layer at the exit of the injector. This interaction was characterized from flame transfer function measurements and chemiluminescence images.

Before any velocity perturbations were imposed, unforced flame chemiluminescence images were examined. It was found that flame length increased with both mean flow velocity and equivalence ratio. There were two general flame shapes observed: a typical "V' flame shape and a longer length "V" flame with an extension into the corner recirculation zone.

Forced flame chemiluminescence images averaged over the entire forcing period yielded similar results to the unforced images. For low velocity forcing amplitudes, it was found that the flame length was constant regardless of forcing frequency. Also at low velocity forcing amplitudes, unforced operating conditions had the same flame length as forced operating conditions.

The flame transfer function (FTF) measurement showed that the FTF gain was affected by flame length, flame shape, and mean flow velocity. For many of the conditions, a forcing frequency of minimum gain, $f_{min}$, was also found. Flame length served to increase the gain of the first peak of the FTF gain versus frequency plot, for frequencies less than $f_{min}$. In addition, the frequency $f_{min}$ increased with increasing flame length. Flame shape governed the appearance of a

second peak in the FTF gain versus frequency plots. In the most extreme case of the longer length "V" flame shape, no $f_{min}$ frequency, and thus no second peak, was observed. Increasing mean flow velocity had a similar but distinct effect of increasing $f_{min}$. Finally, the first peak of the FTF gain plot, the regime with forcing frequencies less than $f_{min}$, could be generalized in terms of $f_{min}$, but the second peak could not. The behavior of the second peak was governed by flame length and flame shape.

Utilizing chemiluminescence images phase synchronized with the inlet velocity perturbation, information about the phase and amplitude of the two flame response mechanisms: mean flame area fluctuations and turbulent flame area fluctuations. It was shown that the two flame response mechanisms could interact constructively or destructively, significantly affecting the global heat release rate response. Their relationship was determined by the forcing frequency and mean flow velocity, in addition to flame shape.

Flames with the longer length "V" flame shape behaved very differently from flames with the typical shorter "V" flame shape. For the longer flames, it was shown that the turbulent flame area fluctuation had a much greater effect on the net heat release response than the mean flame surface area fluctuation. In fact, even though the two flame response mechanisms interacted destructively, it was shown that the effect of the turbulent flame area fluctuation was much larger than that of the mean flame area fluctuation. The reduced fluctuations in the mean flame area are likely to be due to the fact that when the flame is long its mean flame location is constrained by the combustor wall.

Also, the inlet velocity fluctuation magnitude was varied while keeping other operating conditions constant. For the typical "V" flame shape, the velocity forcing amplitude for the onset of heat release response nonlinearity decreased with increasing forcing frequency. As the velocity forcing amplitude was increased at the $f_{min}$ forcing frequency, the two flame response

mechanisms no longer cancelled each other entirely. Finally, vortex shedding was observed at the largest velocity forcing amplitudes.

This study provided insight into the flame heat release response in a lean-premixed, swirl-stabilized, gas turbine combustor. It was shown that the constructive or destructive interaction of the local flame response mechanisms could drastically alter the global flame response.

## 4.2 Suggestions for Future Work

Future work could include:

1) Examination of the effect of centerbody recess on the flame response mechanism interaction. The experimental rig utilized in the present work is a practical industrial nozzle with a centerbody recessed ¾" from the dump plane. This characteristic may have affected the interaction of the flame response mechanisms. To confirm or disprove this, modifying the existing rig by adding an extension to the centerbody to make it flush with the dump plane or conducting experiments on a new rig with similar nozzle and combustor geometry, which excluded the recessed centerbody, would eliminate the influence of centerbody recess.

2) Gathering chemiluminescence image and flame transfer function data for other long length flames and determining whether the flame response mechanism associated with turbulent flame area fluctuations is the dominant premixed flame response mechanism, regardless of experimental rig geometry. A wide combustor which did not restrict the

mean flame location would eliminate the influence of the combustor wall on the mean flame surface area fluctuation.

3) Investigating the slight differences in CH*, $CO_2$*, and OH* flame transfer function gain and phase. In the present work, the species CH* is utilized. As shown in Appendix B, flame transfer function results using OH* differ slightly from CH* results. Flame chemiluminescence images could be taken with an OH* filter and compared to CH* images to search for possible differences in flame response mechanism interaction. $CO_2$* could also be investigated if the appropriate background spectrum is subtracted.

4) Obtaining additional experimental data investigating the effect of the velocity forcing amplitude on the frequency $f_{min}$. Preetham et al. [14] states that the forcing frequency $f_{min}$ will shift to a higher frequency when a greater velocity forcing amplitude is applied to a given operating condition. In Section 3.5, it was shown that, at the forcing frequency $f_{min}$, increasing the velocity forcing amplitude did yield a non-negligible flame response. However, it was not investigated whether or not the frequency $f_{min}$ had actually shifted to a higher forcing frequency.

## Appendix A

# Photomultiplier Tube Calibration Information

Photomultiplier tubes (PMT) record the global flame chemiluminescence intensity. This information is registered as a voltage; the larger the voltage magnitude, the greater the intensity. As long as the PMT remains in the same orientation, the relative magnitudes of the chemiluminescence data from different operating conditions and experiment run times can be compared to each other. If the PMT housing is moved, however, it is difficult to reposition it in exactly the same orientation. Therefore, a calibration curve is obtained. That way, data from the PMT after it has been re-orientated can be compared to data when the PMT was in its original orientation.

To develop this calibration curve, global flame chemiluminescence data is taken from a number of different operating conditions. This data is then used to plot an exponential chemiluminescence intensity versus equivalence ratio calibration curve. The exponential curve fit is used because Lee et al. [5] state that chemiluminescence intensity increases exponentially with equivalence ratio.

Figures **A-1** – **A-4** provide PMT calibration information. Examples of CH* intensity data versus mean velocity for given equivalence ratios 0.70 and 0.75 can be seen in Figures **A-1** and **A-2** respectively. The same information is presented for OH* in Figures **A-3** and **A-4**. For all the figures, the chemiluminescence intensity appears to increase linearly with mean flow velocity. This result is expected. As the mean flow velocity increases, so does the overall fuel flow rate, and Lee et al. [5] mention that chemiluminescence intensity increases linearly with fuel flow rate. Data from both CH* and OH* measurements yield similar trends. Appendix B provides descriptions for the PMT alignment and dates PMT1 and PMT3.

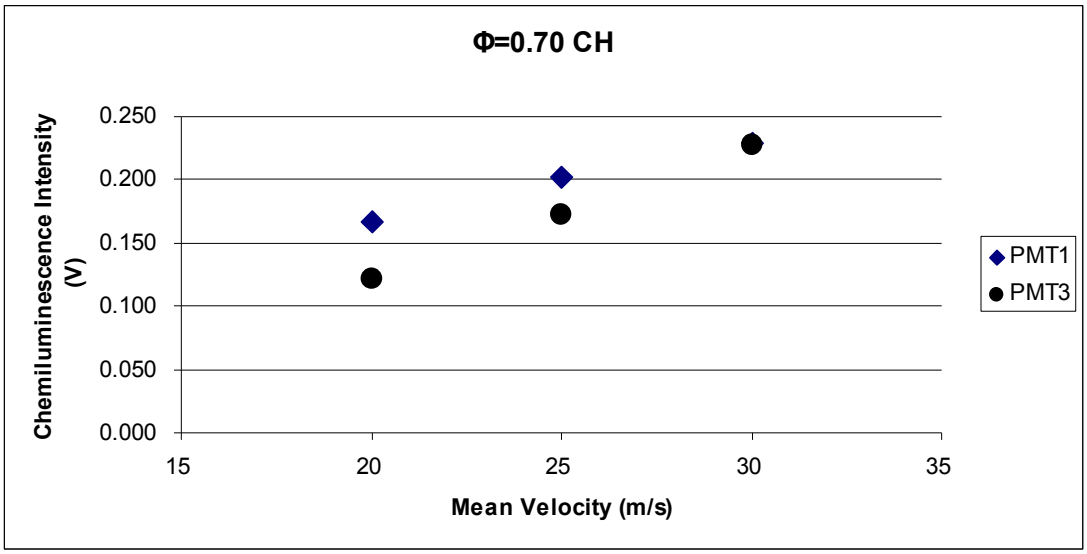


Figure **A-1**: CH* PMT calibration test (a.u.). Operating conditions: $V_{mean}$ = 20 m/s, 25 m/s, and 30 m/s, Φ = 0.70.

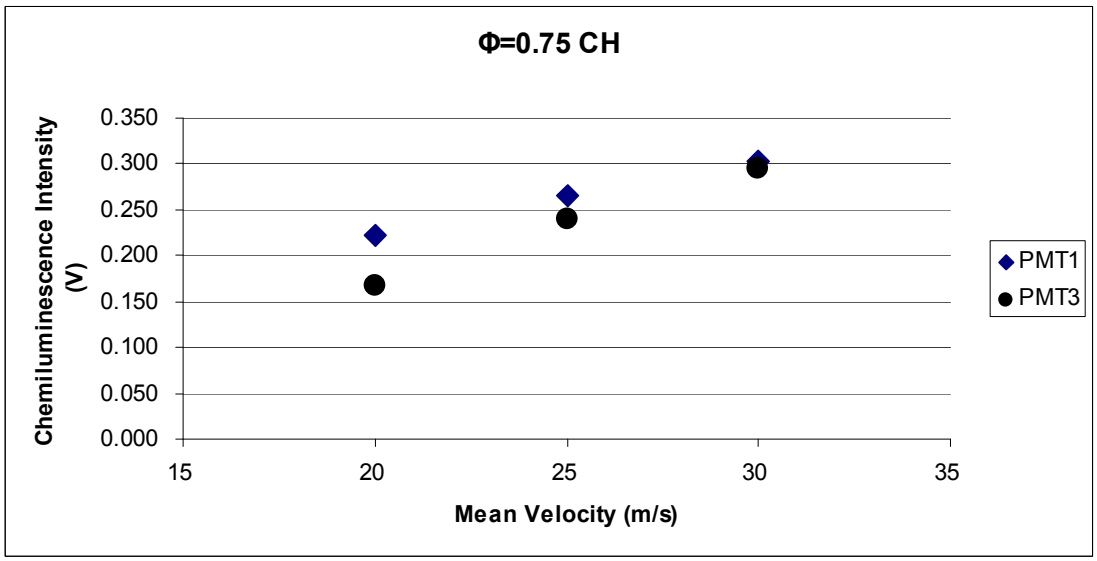


Figure **A-2**: CH* PMT calibration test (a.u.). Operating conditions: $V_{mean}$ = 20 m/s, 25 m/s, and 30 m/s, Φ = 0.75.

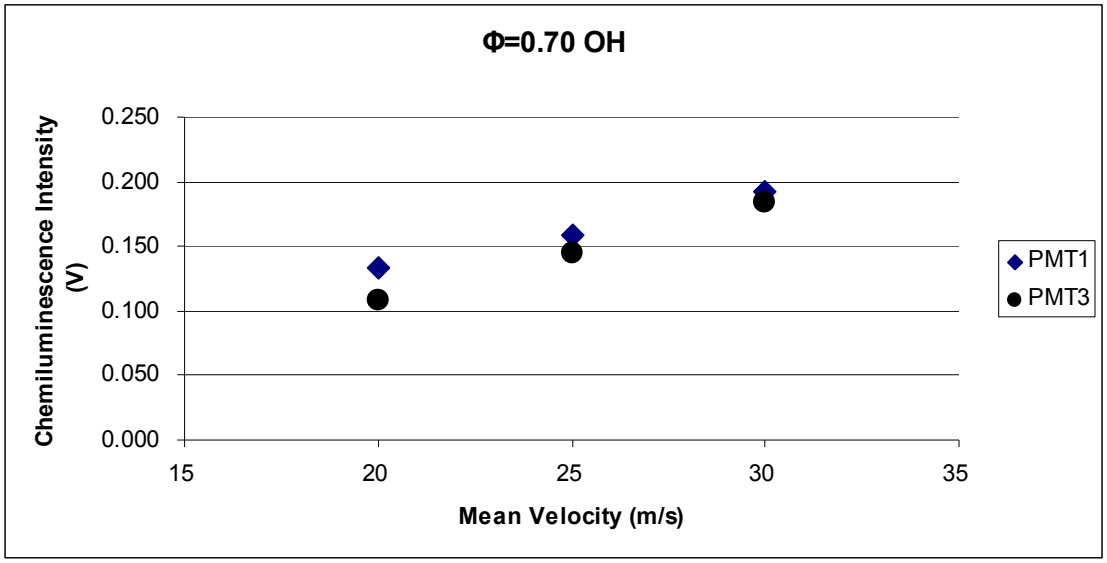


Figure **A-3**: OH* PMT calibration test (a.u.). Operating conditions: $V_{mean}$ = 20 m/s, 25 m/s, and 30 m/s, Φ = 0.70.

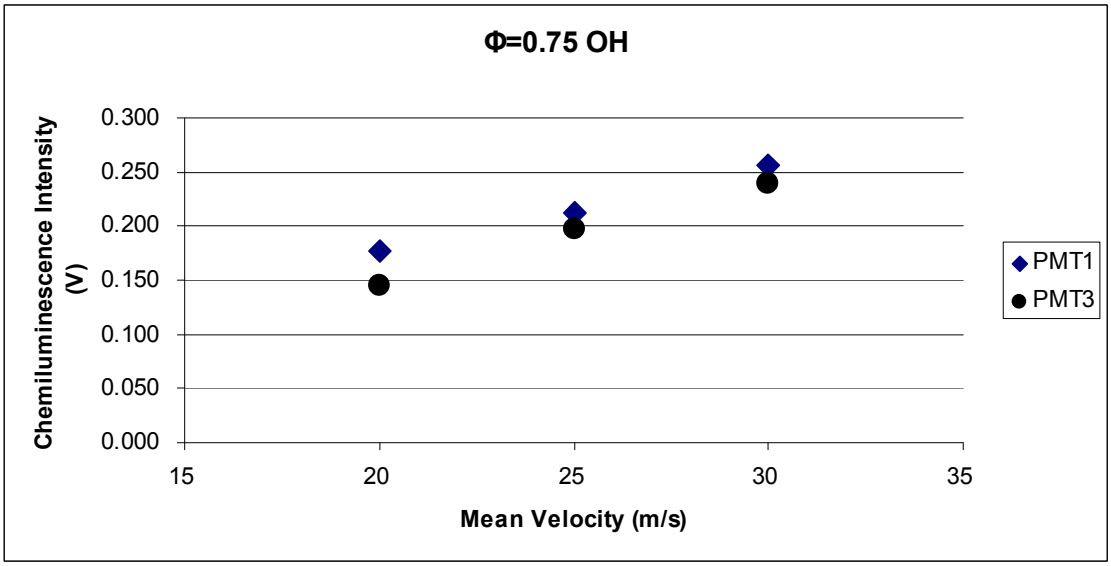


Figure **A-4**: OH* PMT calibration test (a.u.). Operating conditions: $V_{mean}$ = 20 m/s, 25 m/s, and 30 m/s, Φ = 0.75.

## Appendix B

# Flame Transfer Function Measurement Repeatability

Experiments are repeated for the same operating conditions on different days to gauge measurement accuracy. The following figures showcase a set of results for one particular experimental condition $V_{mean}$ = 25 m/s and $\Phi$ = 0.75.

PMT alignments and dates

PMT1: 3/10/2009 – 3/29/2009

PMT3: 5/16/2009 – 6/12/2009

Figures **B-1 – B-5** present data demonstrating the repeatability of the flame transfer function (FTF) results obtained from both CH* and OH* chemiluminescence measurements. For a given PMT calibration (see Section **2.3.3** for PMT calibration information), the magnitudes of the FTF gain measurements are typically within ±4% of the averaged value. Values for CH* gain are shown in Figure **B-1** and OH* gain are shown in Figure **B-3**.

As shown in Figures **B-1**, **B-3**, and **B-5**, the FTF gain for both CH* and OH* is more variable at forcing frequencies greater than $f_{min}$. The gain varies less, within ±1% of the averaged value, at forcing frequencies less than $f_{min}$. Figures **B-2** and **B-4** show that the phase results are repeatable for CH* and OH*, especially for a given PMT calibration.

Finally, Figure **B-5** plots the FTF gain for CH* and OH* for the same operating condition. Overall, the same gain versus frequency profile is observed, but the 1$^{st}$ peak of the OH* gain is slighter larger than that of the CH* gain, and the 2$^{nd}$ peak of the OH* gain is slightly smaller than that of the CH* gain. In this study, it was observed that the magnitudes of the FTF gain results for CH* and OH* are similar. All the data presented in the Results and Discussion section is CH* chemiluminescence data, but similar results could have been found for OH*.

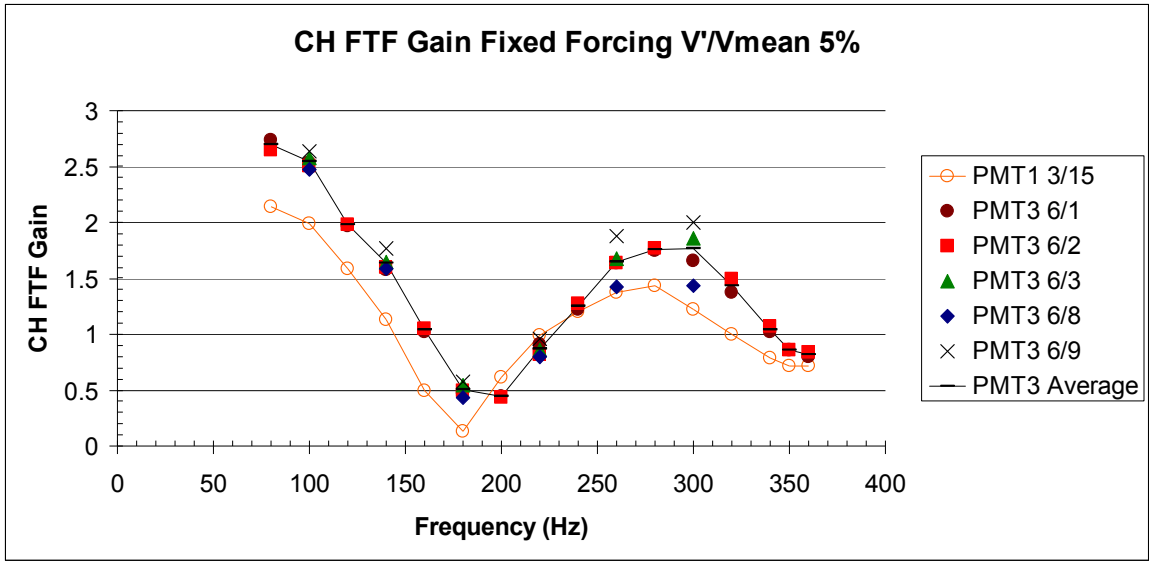


Figure **B-1**: Experiment repeatability CH FTF gain (lines for emphasis). Operating conditions: $V_{mean}$ = 25 m/s, $\Phi$ = 0.75, V'/$V_{mean}$ = 5%, frequency = 80 Hz – 360 Hz.

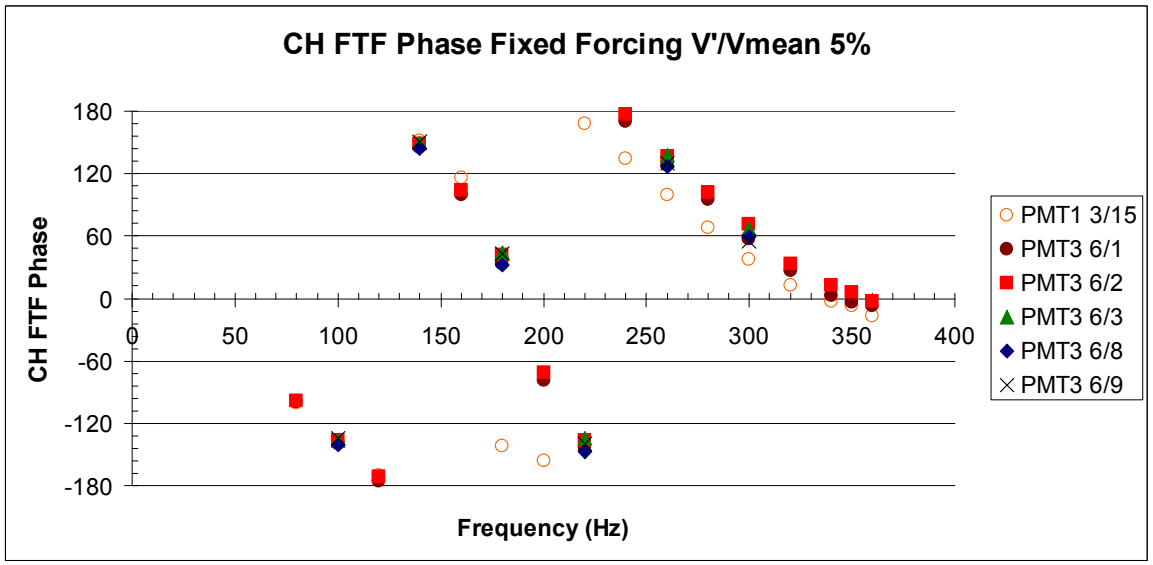


Figure **B-2**: Experiment repeatability CH FTF Phase. Operating conditions: $V_{mean}$ = 25 m/s, $\Phi$ = 0.75, V'/$V_{mean}$ = 5%, frequency = 80 Hz – 360 Hz.

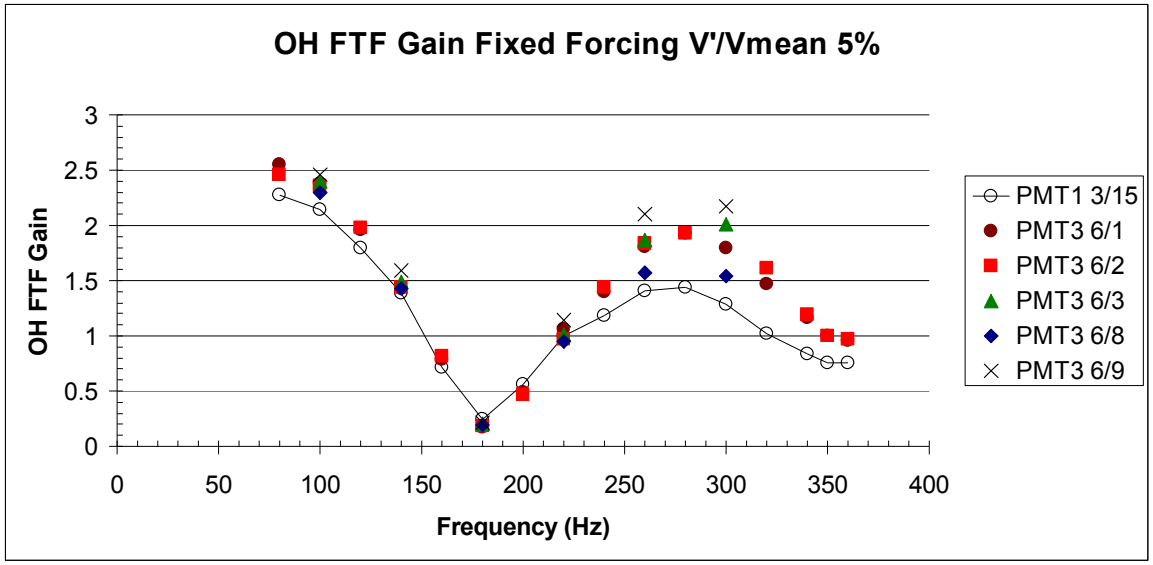


Figure **B-3**: Experiment repeatability OH FTF gain (lines for emphasis). Operating conditions: $V_{mean}$ = 25 m/s, $\Phi$ = 0.75, $V'/V_{mean}$ = 0.05, frequency = 80 Hz – 360 Hz.

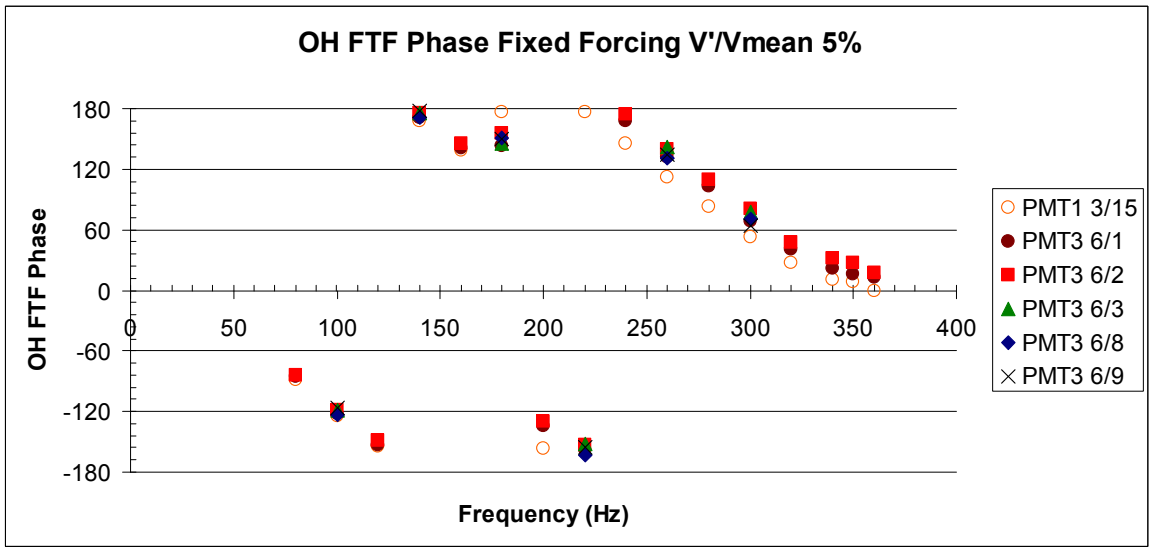


Figure **B-4**: Experiment repeatability OH FTF phase. Operating conditions: $V_{mean}$ = 25 m/s, $\Phi$ = 0.75, $V'/V_{mean}$ = 5%, frequency = 80 Hz – 360 Hz.

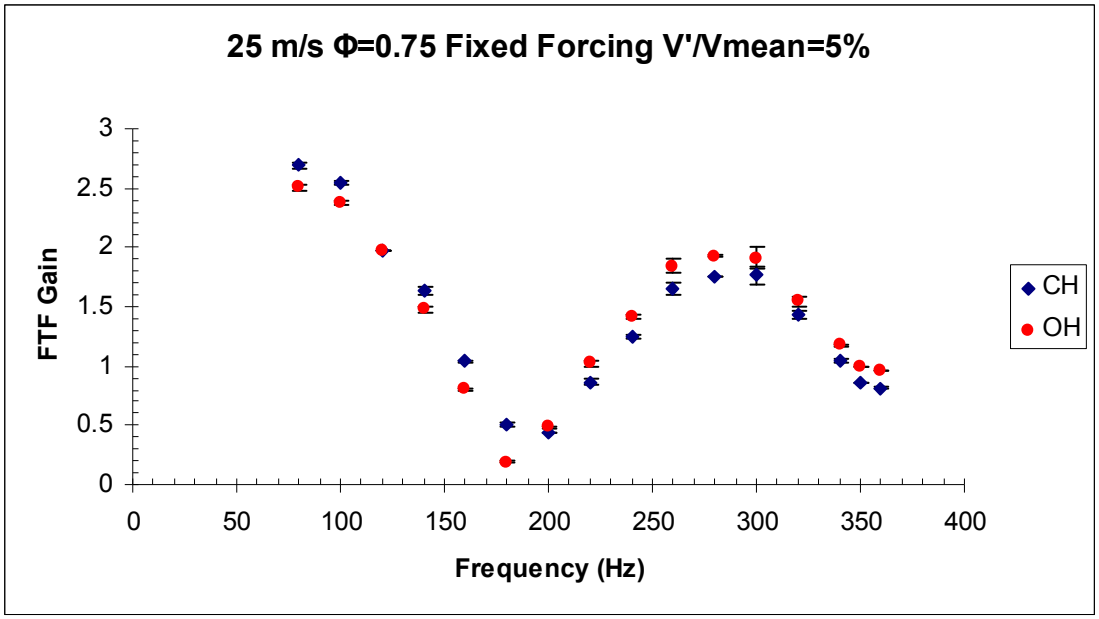


Figure **B-5**: Experiment repeatability FTF gain for CH and OH with error bars. Operating conditions: $V_{mean}$ = 25 m/s, $\Phi$ = 0.70, V'/$V_{mean}$ = 5%, frequency = 80 Hz – 360 Hz.

## References

[1] Correa, S.M., "Power Generation and Aeropropulsion Gas Turbines: From Combustion Science to Combustion Technology," Proceedings of the Combustion Institute, Vol. 27, 1998, pp. 1793-1807.

[2] Correa, S.M., "A Review of NOx Formation under Gas-Turbine Combustion Conditions," Combustion Science and Technology, Vol. 87, 1993, pp. 329-362.

[3] Rayleigh, J.W.S., The *Theory of Sound*, Vol. 2, Dover, New York, 1945.

[4] Goy, C.J., James, S.R., and Rea S., "Monitoring Combustion Instabilities: EON UK's Experience," Chapter 8 in Lieuwen T., Yang, V., editors: Combustion Instabilities in Gas Turbine Engines: Operational Experience, Fundamental Mechanisms, and Modeling, Progress in Astronautics and Aeronautics, 2005, pp. 163-175.

[5] Lee, J.G., and Santavicca, D.A., "Experimental Diagnostics for the Study of Combustion Instabilities in Lean Premixed Combustors," Journal of Propulsion and Power, Vol. 19, No. 5, 2003, pp. 735-750.

[6] Cho, J.H., and Lieuwen, T., "Laminar Premixed Flame Response to Equivalence Ratio Oscillations," Combustion and Flame, Vol. 140, 2005, pp. 116-129.

[7] Polifke, W., and Lawn, C., "On the Low-Frequency Limit of Flame Transfer Functions," Combustion and Flame, Vol. 151, 2007, pp. 437-451.

[8] Balachandran, R., Ayoola, B.O., Kaminski, C.F., Dowling, A.P., and Mastorakos, E., "Experimental Investigation of the Nonlinear Response of Turbulent Premixed Flames to Imposed Velocity Oscillations," Combustion and Flame, Vol. 143, 2005, pp. 37-55.

[9] Bellows, B.D., Neumeier, Y., and Lieuwen, T., "Forced Response of a Swirling, Premixed Flame to Flow Disturbances," Journal of Propulsion and Power, Vol. 22, No. 5, 2006, pp. 1075-1084.

[10] Durox, D., Schuller, T., Candel, S., "Combustion Dynamics of Inverted Conical Flames" Proceedings of the Combustion Institute, Vol. 30, 2005, pp. 1717-1724.

[11] Külsheimer, C., and Büchner, H., "Combustion Dynamics of Turbulent Swirling Flames," Combustion and Flame, Vol. 131, 2002, pp. 70-84.

[12] Schuller, T., Ducruix, S., Durox, D., and Candel, S., "Modeling Tools for the Prediction of Premixed Flame Transfer Functions," Proceedings of the Combustion Institute, Vol. 29, 2002, pp. 107-113.

[13] Sengissen, A.X., Van Kampen, J.F., Huls, R.A., Stoffels, G.G.M., Kok, J.B.W., Poinsot, T.J., "LES and Experimental Studies of Cold and Reacting Flow in a Swirled Partially Premixed Burner with and without Fuel Modulation," Combustion and Flame, Vol. 150, 2007, pp. 40-53.

[14] Preetham, Santosh, H., and Lieuwen, T., "Dynamics of Laminar Premixed Flames Forced by Harmonic Velocity Disturbances," Journal of Propulsion and Power, Vol. 24, No. 6, 2008, pp. 1390-1402.

[15] Polifke, W., and Lawn, C., "On the Low-Frequency Limit of Flame Transfer Functions," Combustion and Flame, Vol. 151, 2007, pp. 437-451.

[16] Schuller, T., Durox, D., and Candel, S., "A Unified Model for the Prediction of Laminar Flame Transfer Functions: Comparisons Between Conical and V-Flame Dynamics," Combustion and Flame, Vol. 134, 2003, pp. 21-34.

[17] Boyer, L., and Quinard, J., "On the Dynamics of Anchored Flames," Combustion and Flame, Vol. 82, 1990, pp. 51-65.

[18] Fleifil, M., Annaswamy, A.M., Ghoneim, Z.A., and Ghoniem, A.F., "Response of a Laminar Premixed Flame to Flow Oscillations: A Kinematic Model and Thermoacoustic Instability Results," Vol. 106, 1996, pp. 487-510.

[19] Dowling, A.P., and Stow, S.R., "Acoustic Analysis of Gas Turbine Combustors," Journal of Propulsion and Power, Vol. 19, 2003, pp. 751-764.

[20] Belluci, V., Shuermans, B., Nowak, D., Flohr, P., and Paschereit, C.O., "Thermoacoustic Modeling of a Gas Turbine Combustor Equipped with Acoustic Dampers," Journal of Turbomachinery, Vol. 127, 2005, pp. 372-379.

[21] Lieuwen, T., "Nonlinear Kinematic Response of Premixed Flames to Harmonic Velocity Disturbances," Proceedings of the Combustion Institute, Vol. 30, 2005, pp. 1725-1732.

[22] Kim, K.T., Lee, J.G., Lee, H.J., Quay, B.D., and Santavicca, D.A., "Characterization of Forced Flame Response of Swirl-Stabilized Turbulent Premixed Flames," accepted for publication in Trans. ASME Turbo Journal of Engineering for Gas Turbines and Power (2010).

[23] Santosh, H., Preetham, and Lieuwen, T., "Response of Turbulent Premixed Flames to Harmonic Acoustic Forcing," Proceedings of the Combustion Institute, Vol. 31, 2007, pp. 1427-1434.

[24] Noiray, N., Durox, D., Schuller, T., and Candel, S., "A Unified Framework for Nonlinear Combustion Instability Analysis Based on the Flame Describing Function," Journal of Fluid Mechanics, Vol. 615, pp. 139-167, 2008.

[25] Chaudhuri, S., Cetegen, B.M., "Response Dynamics of Bluff-body Stabilized Conical Premixed Turbulent Flames with Spatial Mixture Gradients," Combustion and Flame, Vol. 156, 2009, pp. 706-720.

[26] Kim, D., Lee, J.G., Quay, B.D., and Santavicca, D.A., "Effect of Flame Structure on the Flame Transfer Function in a Premixed Gas Turbine Combustor," accepted for publication in Trans. ASME Journal of Engineering for Gas Turbines and Power, 2010.

[27 ] Miller, S.A., Development of a Flame Chemiluminescence Probe for Determination of Primary Zone Equivalence Ratio in Gas Turbine Combustors, M.S. Thesis, Department of Mechanical and Nuclear Engineering, The Pennsylvania State University, 1999.

[28] Dasch, C.J., "One-Dimensional Tomography: A Comparison of Abel, Onion-Peeling, and Filtered Backprojection Methods," Applied Optics, Vol. 31, No. 8, 1992, pp. 1146-1152.

[29] Lieuwen T., "Modeling Premixed Combustion-Acoustic Wave Interactions: A Review," Journal of Propulsion and Power, Vol. 19, No. 5, 2003, pp. 765-781.

[30] Barker, A., Carrotte, J., and Denman, P., "Analysis of Hot-Wire Anemometry Data in an Acoustically Excited Turbulent Flow Field," Experiments in Fluids, Vol. 39, 2005, pp. 1061-1070.

[31] Nottin, C., Knikker, R., Boger, M., and Veynante, D., "Large Eddy Simulations of an Acoustically Excited Turbulent Premixed Flame," Proceedings of the Combustion Institute, Vol. 28, 2000, pp. 67 – 73.

[32] Jones, B., Lee, J.G., Quay, B.D., and Santavicca, D.A., "Flame Response Mechanisms Due to Velocity Perturbations in a Lean Premixed Gas Turbine Combustor," Journal of Engineering for Gas Turbines and Power, Vol. 133, No. 2, February 2011.

[33] Bellows, B.D., Bobba, M.K., Seitzman, J.M., and Lieuwen, T., "Nonlinear Flame Transfer Function Characteristics in a Swirl-Stabilized Combustor," Journal of Engineering for Gas Turbines and Power, Vol. 129, 2007, pp. 954-961.